

# An enstrophy-based analysis of the turbulence–interface interactions across the scales

Mahdi Saeedipour\*

Department of Particulate Flow Modelling, Johannes Kepler University, A-4040 Linz, Austria  
Linz Institute of Technology (LIT), Johannes Kepler University, A-4040 Linz, Austria

## ARTICLE INFO

### Keywords:

Multiphase turbulence  
Liquid–gas flow  
Turbulent breakup  
Fragmentation  
VOF method  
Direct numerical simulation

## ABSTRACT

This study presents an analysis of the turbulence–interface interactions during the sheet fragmentation process based on the concept of enstrophy transport across the length scales. We carried out fully-resolved volume of fluid (VOF) simulations of the decaying homogeneous isotropic turbulence (HIT) in the presence of an initially flat sheet of interface and analyzed the spectral rates of enstrophy production/destruction due to different mechanisms in the enstrophy transport equation. We highlight the scale-dependent nature of the surface tension mechanism that interacts with the vortex stretching term and shapes the evolution of interfacial turbulence. It is demonstrated that the spectral rate of surface tension term in enstrophy transport equation changes sign at a characteristic length scale distinguishing between the nature of interfacial events: negative for enstrophy-reducing fragmentation and positive for enstrophy-releasing surface minimization and coalescence. We further show that at another characteristic length scale, the rate of enstrophy production by the surface tension balances the disruptive mechanism of vortex stretching. This corresponds to a similar length scale that the energy cascade of two-phase turbulence deviates from its single-phase similitude, and is also similar to the length scale at which the size distribution of droplets distinctly changes to a sharper slope. The analysis further discloses that increasing sheet Weber number by lowering the surface tension coefficient, increasing density, and decreasing the viscosity of the sheet all enhance the vortex stretching effect across the scales and dilate the spectral range at which the surface tension contribution is negative toward the smaller scales, and thus facilitate the fragmentation. Whereas the higher surface tension coefficient, higher viscosity, and lower density ratio expand the spectral range associated with a positive contribution of surface tension toward the larger scales and suppress fragmentation events. This enstrophy-based description offers a new interpretation of the range of maximum stable droplets in turbulence. Accordingly, an approximation is proposed and tested for the Hinze scale in present configuration which could serve as the basis for future developments in DNS and LES of two-phase flows.

## 1. Introduction

Atomization, liquid disintegration and emulsification are multiphase processes that recur in many real-life engineering applications. When two coexisting immiscible fluids encounter instabilities, due to the imbalance of disruptive and consolidating mechanisms, one fluid element may fragment into many smaller ones (Villermaux, 2007). Flow inertia, further intensified by turbulence, is known as a major disruptive effect, whereas the surface tension at the fluid–fluid interface is the major resistance to the fragmentation. Turbulent interfacial flows are the common ground for such physical competition that results in generation of interfacial structures such as droplets and bubbles. Therefore, turbulence–interface interactions play the integral role in

shaping the fragmentation characteristics, and control the droplet size distribution of turbulent atomization and liquid emulsification.

The well-known limitations and complexities of the experimental characterization of turbulent interfacial flows make the numerical simulation a prominent tool for investigation. Despite the progress of computational power in turbulence research, the direct numerical simulation (DNS) of multiphase flows is still a big challenge due to excessive demands for grid resolution and conceptual dispute about the required criterion for referring as *fully-resolved* simulations (Estivalezes et al., 2022; Saeedipour et al., 2021). This explains why large eddy simulation (LES) and coarse-grid multiscale methods have gained a lot of attention for the simulation of atomization and emulsification processes (Vincent et al., 2018; Saeedipour et al., 2019; Klein et al.,

\* Correspondence to: Department of Particulate Flow Modelling, Johannes Kepler University, A-4040 Linz, Austria.  
E-mail address: [mahdi.saeedipour@jku.at](mailto:mahdi.saeedipour@jku.at).

2019; Ling et al., 2015; Saeedipour et al., 2017). These methods share the principal concept of subgrid-scale (SGS) modeling i.e. proposing a model for small-scale, unresolved-by-grid physics applicable to the range of scales below a cut-off length (grid resolution). Nevertheless, the current state-of-the-art two-phase LES methods lack physical closure models for the unresolved surface tension and its interactions with turbulence across the scales that influence interfacial events such as breakup and coalescence (for more details on the shortcomings of the two-phase LES models and their limitations, we refer to Klein et al. (2019), Hasslberger et al. (2020) and Saeedipour and Schneiderbauer (2019) and the references therein).

Thus, an in-depth physical understanding of turbulence–interface interactions across the scales is required to develop more accurate functional closure models. Recent studies have demonstrated that the surface tension negatively contribute to the turbulence energy cascade at larger scales of the spectrum, while it acts as the source for the turbulent kinetic energy (TKE) at the smaller scales, and therefore, the interfacial structures cause the turbulence energy cascade to deviate from the classical single-phase turbulence (Saeedipour et al., 2019; Schneiderbauer and Saeedipour, 2022; Crialesi-Esposito et al., 2022; Saeedipour and Schneiderbauer, 2022). This scale-dependent nature of modulations mandates the determination of some characteristic length scales for the interfacial structures to set appropriate spatial resolutions (Jofre et al., 2020) and assess the applicability of such closure models.

In the context of turbulence-driven fragmentation, a relevant characteristic length-scale is the Hinze scale  $d_H$  (Hinze, 1955), which represents the maximum size of stable droplets generated in turbulence. It is well-studied in the literature that interaction of droplets in homogeneous isotropic turbulence (HIT) promote a fragmentation cascade with existing power-law correlations for the size distribution of sub- and super-Hinze droplets (Deane and Stokes, 2002). Recent DNS studies of emulsification of droplets in non-decaying HIT could exhibit these power-law correlations mostly for sub-Hinze droplets (Crialesi-Esposito et al., 2022; Begemann et al., 2022). Nevertheless, the original definition of  $d_H$  contains a critical Weber number that might be case-dependent and may limit its generality for different problems. This motivates further exploration on this characteristic length scale which is one of the objectives of the present study.

Recently, we have described the multiphase turbulence phenomena based on the concept of vorticity transport and the evolution of vortical energy across the scales i.e. enstrophy (Saeedipour and Schneiderbauer, 2022). We analyzed the spectral contribution of the rate of different vorticity generation/destruction mechanisms and observed some critical length scales where the energy/enstrophy cascades of a multiphase turbulent flow deviates from its single-phase ones. Our analysis reveals that these critical length scales represent a characteristic size of eddies for which the vortex stretching mechanism is unable to drive the cascade further, and the eddy breakup events do not contribute to the energy transfer at small scales. Following this enstrophy-based description, we believe these critical length scales may correspond to the size of stable droplets during the decaying isotropic turbulence. In other words, they may represent the maximum size of droplets where the enstrophy imbalance is always in favor of the surface tension, preventing from further breakup. While this reminisces the very definition of the Hinze scale, it is still subject to further quantitative evaluations.

In the present study, we investigate the turbulence–interface interactions in a freely decaying HIT using fully-resolved volume of fluid (VOF) simulations. The problem configuration is similar to our previous research (Saeedipour and Schneiderbauer, 2021, 2022) that allows to study the temporal evolution of the interfacial turbulence from an initially-flat interface until the dispersed droplet-laden flow. We base our analysis on spectral contribution of different mechanisms in enstrophy transport. As an extension to the previous works, we also account for the density and viscosity contrasts between the phases, to find out how they influence the temporal and spectral characteristics of the interfacial turbulence. The originality of the present study is

twofold: (i) we describe the turbulence–interface interactions in interfacial flows with complexities based on the concept of enstrophy generation/destruction, and (ii) we identify and connect the critical length scales of this enstrophy-based analysis to the statistics of the dispersed two-phase flow. While the former enriches the understanding of the underlying physics which is necessary to shape new functional SGS models for two-phase LES, the latter could pave the path toward a more deterministic interpretation for the Hinze scale.

This paper is structured as follows. In Section 2, we present the governing equations, theoretical background, and principles required to perform numerical simulations and carry out the analysis. Section 3 introduces the details of the numerical setup for the fully-resolved simulations. The results of this enstrophy-based analysis are presented in different steps within Section 4. The paper ends with the conclusions in Section 5.

## 2. Theory and principles

### 2.1. Governing equations of the incompressible two-phase flow

The unsteady motion of an incompressible, immiscible, two-phase flow can be described by the one-fluid formulation comprising the continuity and Navier–Stokes equations together with an additional transport equation for the interface capturing technique. This additional equation determines the interface between the phases by tracking a phase indicator scalar field  $\alpha$ , which, in VOF method, corresponds to the volume ratio of primary phase to the whole computational cell volume. This system of equations reads

$$\nabla \cdot \mathbf{u} = 0 \quad (1)$$

$$\frac{\partial(\rho\mathbf{u})}{\partial t} + \nabla \cdot (\rho\mathbf{u} \otimes \mathbf{u}) = -\nabla p + \nabla \cdot \boldsymbol{\tau} + \rho\mathbf{g} + \mathbf{f}_\sigma \quad (2)$$

$$\frac{\partial\alpha}{\partial t} + \nabla \cdot (\alpha\mathbf{u}) = 0 \quad (3)$$

where  $\mathbf{u}$  is the mixture velocity vector shared with both phases,  $p$  is the pressure, and  $\boldsymbol{\tau} = \mu[(\nabla\mathbf{u}) + (\nabla\mathbf{u})^T]$  is the viscous stress tensor. The material properties such as density and viscosity are determined by  $\alpha$  based on a mixture assumption as  $\rho = \alpha\rho_1 + (1 - \alpha)\rho_2$  and  $\mu = \alpha\mu_1 + (1 - \alpha)\mu_2$ . The gravitational acceleration vector is denoted by  $\mathbf{g}$ , and the last term represents the surface tension force that is commonly computed by the Continuous Surface Force (CSF) method (Brackbill et al., 1992), and reads  $\mathbf{f}_\sigma = \sigma\kappa\hat{\mathbf{n}}\delta_s$ . In this formulation  $\sigma$  is the surface tension coefficient,  $\hat{\mathbf{n}} = \frac{\nabla\alpha}{|\nabla\alpha|}$  is the interface unit normal vector, and interface curvature is approximated by  $\kappa = -\nabla \cdot \hat{\mathbf{n}}$ . Also,  $\delta_s \equiv |\nabla\alpha|$  is the mathematical delta function that equals infinity at the interface and zero elsewhere. In the context of finite volume CFD, the numerical solution of this system of equations is supposed to resolve all the flow scales when sufficiently-high grid resolutions and advanced algorithms are employed.

### 2.2. Vorticity and enstrophy transport equations

In fluid dynamics, vorticity ( $\boldsymbol{\omega} = \nabla \times \mathbf{u}$ ) is a vector quantity associated with rotational motions in fluid, and consequently could serve as a physical descriptor of the dynamics of vortical structures i.e. eddies in turbulence. Particularly, the hierarchical cascading process in turbulence and the energy transfer across the length scales could be described in accordance with the mechanisms involved in vorticity transport phenomenon (McComb, 1992; Pope, 2000). The vorticity transport equation is derived by taking the curl of Eq. (2).

$$\begin{aligned} \frac{D\boldsymbol{\omega}}{Dt} &= (\boldsymbol{\omega} \cdot \nabla)\mathbf{u} + \nu\nabla^2\boldsymbol{\omega} \\ &\quad - \frac{\nabla\rho}{\rho^2} \times \nabla \cdot \boldsymbol{\tau} + \frac{\nabla\rho}{\rho^2} \times \nabla p + \nabla \times \left( \frac{\sigma}{\rho} \kappa \hat{\mathbf{n}} \delta_s \right). \end{aligned} \quad (4)$$

The first two terms on the right-hand side (RHS) of Eq. (4) are the vortex stretching ( $T_{VS}$ ) and viscous dissipation ( $T_D$ ) terms. Similar to

the single-phase turbulent flows, these mechanisms play essential roles in cascading process. For incompressible multiphase flows, the other three terms on the RHS of vorticity equation appear solely because of the multiphase nature of the flow. The third term corresponds to the vorticity destruction due to the misalignment of the density gradient vector and viscous stresses, which is also known as viscous torque ( $T_V$ ). The fourth term is usually referred as the baroclinic torque ( $T_B$ ) that is the vorticity generation/destruction due to the misalignment between the density gradient vector and pressure gradient. Finally, the last term corresponds to the vorticity production/destruction by the surface tension force at the interface region ( $T_\sigma$ ). Due to the alignment of density and volume fraction gradients as well as given the fact that the curl of a gradient of a scalar is zero, this term reduces to

$$T_\sigma = \frac{\sigma}{\rho} \nabla \kappa \times \nabla \alpha, \quad (5)$$

which contains no density gradient (Hasslberger et al., 2018) and is solely dependent on the interface geometry i.e. curvature and normal vector. This implies that the geometrical changes in the interface contribute to the vorticity generation close to the interface.

Enstrophy is the vorticity squared ( $\mathcal{E} = \omega \cdot \omega$ ) (Pope, 2000), and represents a scalar quantity that intrinsically reflects the strength of the vorticity field without a vector implication (Denaro, 2018). Therefore, it could serve as a measure for the vortical energy of the turbulent structures. The enstrophy transport equation is derived by the dot product of Eq. (4) with  $\omega$ . Nevertheless, we base our analysis on the spectral distribution of the enstrophy. In the spectral space, the Fourier transform of the enstrophy equation for the two-phase flows reads

$$\frac{d\mathcal{E}(\kappa)}{dt} = \Psi_{VS} + \Psi_D + \Psi_V + \Psi_B + \Psi_\sigma, \quad (6)$$

where  $\Psi$  denotes the rate of the contribution of each vorticity transport mechanism to the enstrophy transported by the eddies across the wavenumbers  $\kappa$ , and is computed by

$$\Psi_i(\kappa, t) = \sum_{\kappa < |\kappa| < \kappa+1} \hat{\omega}(\kappa, t) \circ \hat{T}_i(\kappa, t). \quad (7)$$

Here,  $T_i$  corresponds to different terms on the right-hand-side of Eq. (4), “ $\hat{\cdot}$ ” is the Fourier transform, and “ $\circ$ ” is the dot product of two complex vectors. It has to be noted that  $\Psi$  has the physical unit of  $[T^{-3}]$  and represents the rate of enstrophy generation/destruction by each mechanism involved in vorticity transport equation, and therefore is employed as the major descriptor of our analysis in this study.

### 2.3. Characteristic scales in interfacial turbulence

From statistical viewpoint, the fragmentation process due to the turbulence–interface interactions results in a wide range of droplet/bubble sizes that, in the case of HIT, feature a characteristic size commonly referred as Hinze scale ( $d_H$ ). This length scale represents the maximum size of stable droplets that are not subject to further breakup. Based on the concept of critical Weber number ( $We = \rho_1 u^2 \delta / \sigma$ ) and using the Kolmogorov theory, Hinze (1955) proposed the following correlation

$$d_H = (We_{cr}/2)^{3/5} (\rho_c/\sigma)^{-3/5} \varepsilon^{-2/5} \quad (8)$$

where  $We_{cr} = 1.17$  is applied to fit experimental data. This length scale has been the basis for further characterization of probability density function (PDF) of droplets generated in HIT. The droplets smaller than this size (i.e. sub-Hinze droplets with  $d < d_H$ ) are resistant to fragmentation and may only be prone to coalescence. Their PDF follow a  $d^{-3/2}$  power law (Deane and Stokes, 2002), and their interaction with isotropic turbulence is interpreted as the source of TKE (Trontin et al., 2010; Dodd and Ferrante, 2016; Saeedipour et al., 2021) due to positive work of surface tension in surface minimization, and the creation of small-scale vortical structures (Saeedipour and Schneiderbauer, 2022; Cialesi-Esposito et al., 2023). The droplets with  $d \geq d_H$

are subject to breakup, which is interpreted as the sink of TKE (Dodd and Ferrante, 2016), and form a sharper slope of  $d^{-10/3}$  in their size distribution spectrum (Garrett et al., 2000). Various DNS studies of the emulsification process in non-decaying HIT have demonstrated these power laws for the PDF of generated droplets (Skartlien et al., 2013; Cialesi-Esposito et al., 2022; Begemann et al., 2022). Nevertheless, the original correlation for  $d_H$  contains case-dependent critical Weber number that needs turning, and relying on the power laws to find the  $d_H$  may be uncertain as the PDF slope transition from  $-3/2$  to  $-10/3$  may only be observed in certain volume fractions (Cialesi-Esposito et al., 2022). Thus, a more general definition for this characteristic seems crucial, which in turn, requires a more in-depth picture of the turbulence evolution across the length scales.

In multiphase turbulent flows, the turbulent kinetic energy follows an intrinsically different cascade process compared to the single-phase turbulence. A couple of previous studies in the literature have underlined this fact by numerical simulations of HIT problems in presence of a flat interface sheet or multiple droplets (Li and Jaber, 2009; Trontin et al., 2010; McCaslin and Desjardins, 2014; Dodd and Ferrante, 2016; Schneiderbauer and Saeedipour, 2022; Saeedipour and Schneiderbauer, 2022; Cialesi-Esposito et al., 2022). Despite using different ways of interpretation, they all have drawn a similar conclusion implying that the presence of interface leaves its footprints on the cascade through the work done by the surface tension (Saeedipour and Schneiderbauer, 2019). As schematically depicted in Fig. 1(a), the difference between the energy cascades in the presence and absence of the interfacial structures is scale-dependent. At low wavenumbers, the large-scale deformations and breakup of the interface extract the kinetic energy from the two-fluid flow due to the surface tension. But at small scales, this energy is given to the flow through the energy-releasing interfacial processes like coalescence. Thus, the high-wavenumber motions (i.e.  $\kappa > \kappa_c$ ) contain a higher amount of energy compared to the same range in the single-phase cascade. The length scale associated with the beginning of this positive deviation in cascade,  $2\pi/\kappa_c$ , is a characteristic length scale at which the interface breakup (sink of energy) is prevented, and the surface tension work starts to become a source of kinetic energy.

For better understanding the underlying physics, we have recently explained this deviation in energy cascade using the vorticity transport equation (Saeedipour and Schneiderbauer, 2022). We focused on the vorticity generation at large- and small-scale motions and could demonstrate that the energy damping effect at large-scale motions is attributed to the negative rate of contribution of surface tension to the enstrophy generation ( $\Psi_\sigma < 0$ ), whereas at smaller scales,  $\Psi_\sigma > 0$  indicating that the misalignment between the gradient of curvature and gradient of volume fraction generates eddies that do not counteract the local vorticity vector, so they positively contribute to enstrophy generation. This is schematically illustrated in Fig. 1(b). This highlights the scale-dependent nature of the surface tension mechanism that characterizes the nature of interfacial events:  $\Psi_\sigma < 0$  implies enstrophy-reducing fragmentation events, while  $\Psi_\sigma > 0$  represents enstrophy-releasing consolidating effect through the surface minimization and coalescence. The wavenumber at which  $\Psi_\sigma$  changes its sign is denoted by  $\kappa_s$ , and could be interpreted as a border between fragmenting and non-fragmenting interfacial scales.

We further show that there is another characteristic wavenumber larger than  $\kappa_s$ , at which the already-positive  $\Psi_\sigma$  start to become larger than the rate of enstrophy generation by the vortex stretching mechanism (i.e.  $\Psi_\sigma > \Psi_{VS}$ ). This wavenumber is denoted by  $\kappa_c$ , and as an important conclusion we could demonstrate that  $\kappa_c \cong \kappa_e$ . In other words, the energy pile up at large wavenumbers begins after the vortex stretching rate becomes weaker compared to the rate of enstrophy production by the surface tension mechanism, and the eddy breakup events are less effective in generating smaller structures. Instead, the surface tension becomes dominant and creates vortical structures through the

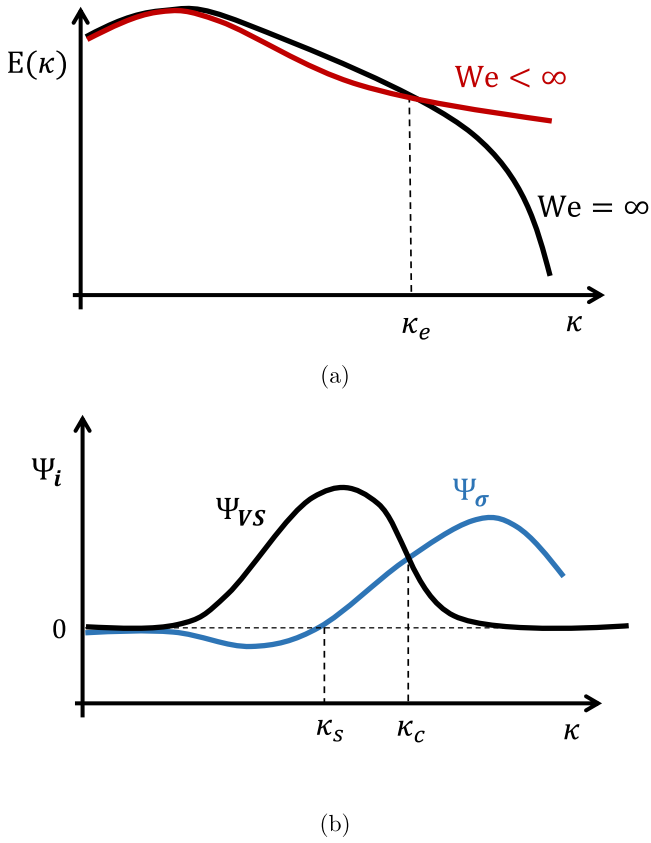


Fig. 1. (a) Schematic form of the energy spectra of single-phase HIT (black) compared with the two-phase HIT (red). The single-phase HIT is referred to as  $We = \infty$  similar to Trontin et al. (2010), (b) schematic illustration of the trends in rate of enstrophy transport by surface tension ( $\Psi_\sigma$ , colored in blue) and vortex stretching mechanism ( $\Psi_{VS}$ , colored in black) inspired from Saeedipour and Schneiderbauer (2022). (For interpretation of the references to color in this figure legend, the reader is referred to the web version of this article.)

act of surface minimization and/or coalescence. This important conclusion implies that turbulent structures smaller than  $2\pi/\kappa_c$  are mainly produced by surface tension mechanism and increase the TKE. This enstrophy-based description reminisces the definition of Hinze scale which distinguishes between the fragmentation-dominated interfacial structures from those stable ones that withstand the turbulent fragmentation, and act as the source of energy/enstrophy. Therefore, seeking a connection between these concepts seems a credible approach toward a more accurate definition of the Hinze scale. Crialesi-Esposito et al. (2023) have recently made such attempt by performing a series of DNS-VOF simulations of emulsification in forced HIT. They compared the spectral contribution of surface tension force to the TKE with the PDF of the generated droplets, and could demonstrate that the change in power law slopes from  $-3/2$  to  $-10/3$  occurs at a length scale associated with  $\kappa_s$  in Fig. 1(b). It has to be noted that their criterion comes from the evaluation of the energy equation in spectral space, and points out the length scale where  $\sum_{\kappa < |\kappa| < \kappa+1} (\hat{u}(\kappa, t) \circ \hat{f}_\sigma(\kappa, t)) \rightarrow 0$ . But it can be mathematically shown that this matches the wavenumber where  $\Psi_\sigma = 0$  in Fig. 1(b). Despite the validity of this approach that ends up with a reasonable range for the Hinze scale, the choice of  $\kappa_s$  may overlook the following physical observations: (i) the positive deviation in cascades starts around  $\kappa_c$  (Saeedipour and Schneiderbauer, 2022), and (ii) the disruptive mechanism of vortex stretching may still be effective for droplet breakup even at  $\kappa > \kappa_s$ , in particular for liquid–liquid systems with large density contrast.

Hence, we believe that the actual Hinze scale may lie within the range of  $\kappa_s \leq 2\pi/d_H \leq \kappa_c$ , and as the lower limit,  $\kappa_c$  (associated

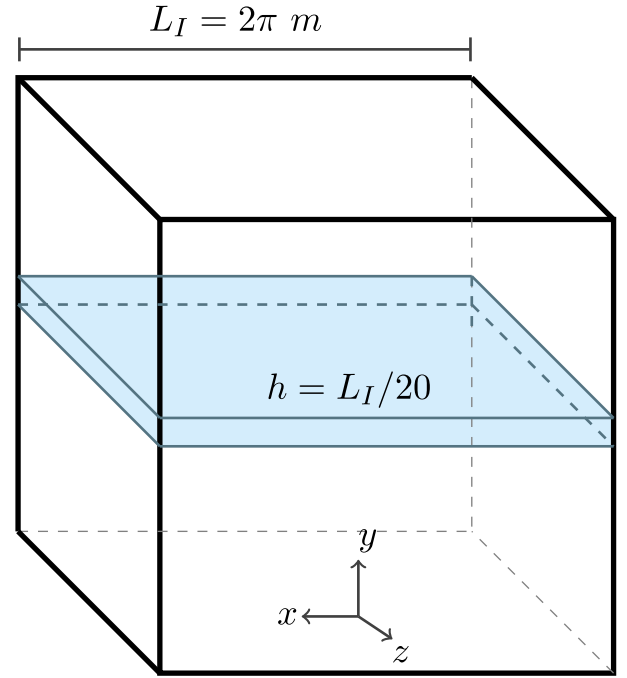


Fig. 2. Schematic of the simulation setup for the two-phase interfacial HIT problem. The thin sheet of interface is located in the center of the box with 5% total volume fraction. The surrounding walls are periodic in each direction.

with  $\Psi_\sigma \cong \Psi_{VS}$ .) could be a more relevant threshold for the stable droplets needed for numerical modeling. In this study, we evaluate this argument and analyze how  $\kappa_s$  and  $\kappa_c$  vary with the different flow parameters.

### 3. Numerical simulation

To investigate the turbulence–interface interactions across the scales and explore the characteristics of the fragmentation, we focus on freely decaying homogeneous isotropic turbulence in the presence of an initially-flat liquid sheet. We carried out fully-resolved numerical simulation of a decaying HIT box similar to our previous studies (Saeedipour and Schneiderbauer, 2021, 2022). This setup is identical to the DNS study of Trontin et al. (2010) and comprises a fully-periodic square box with the length of  $L_I = 2\pi$  m initialized with a specific energy spectrum that, based on their grid dependency analysis, can be fully resolved with  $N = 512^3$  number of uniform finite volume cells. A thin sheet of interface is placed in the center of the box with a thickness of  $\delta = L_I/20$  as schematically illustrated in Fig. 2. This results in a interfacial HIT with 5% total volume fraction. In the remainder of this paper, the sheet and the surrounding fluid are referred to as the dispersed phase and carrier phase, respectively.

A decaying homogeneous isotropic turbulence is generated in this domain as a function of wavenumber ( $\kappa$ ) with the initial energy spectrum of

$$E(\kappa) = \frac{R^2}{2A\kappa_p^{\gamma+1}} \kappa^\gamma \exp\left(-\frac{\gamma}{2} \left(\frac{\kappa}{\kappa_p}\right)^2\right), \quad (9)$$

where  $\kappa_p$  is the wavenumber at maximum  $E(\kappa)$ . The constant parameters are all set similarly to Trontin et al. (2010) i.e.  $R^2 = 3$ ,  $\gamma = 4$ ,  $\kappa_p = 9$  and  $A = 0.11$ . This initial turbulence entails a velocity scale of  $u' = 1$  m/s and the Kolmogorov length scale (i.e. smallest resolvable scale) of  $\eta = 0.01312$  m. The density and viscosity ratios between the phases are equally set to one with the values of  $\rho_1 = \rho_2 = 1$  kg/m<sup>3</sup> and  $\mu_1 = \mu_2 = 0.003$  Pa s. Accordingly, the initial Taylor-scale Reynolds number of  $Re_\lambda = 74$  (where  $Re_\lambda = \rho_1 u' \lambda / \mu_1$ ). The surface

**Table 1**

Simulation cases of interfacial two-phase HIT considered in this study. The dimensionless numbers are computed based on the dispersed phase properties and sheet thickness ( $\delta$ ).

Cases	$r = \rho_1/\rho_2$	$m = \mu_1/\mu_2$	$\sigma$	$We_\delta$	$Re_\delta$
C-1 (ref)	1	1	$2.85 \times 10^{-3}$	110	105
C-2	1	1	$4.98 \times 10^{-3}$	63	105
C-3	1	1	$1.42 \times 10^{-3}$	220	105
C-4	0.1	1	$2.85 \times 10^{-3}$	11	10.5
C-5	10	1	$2.85 \times 10^{-3}$	1100	1050
C-6	1	0.1	$2.85 \times 10^{-3}$	110	1050
C-7	1	0.01	$2.85 \times 10^{-3}$	110	10500

tension coefficient  $\sigma$  is varied to account for different Weber numbers  $We = \rho_1 u^2 \delta / \sigma$ .

In this study, we first keep the density and viscosity values unchanged and focus on the variation of  $\sigma$  that leads to three different  $We$  numbers of 63, 110, and 220. Since the primary objective of this study is to assess the proposed enstrophy-based approach to the characterization of the dispersed phase in decaying turbulence, the Weber numbers are chosen relatively high to ensure that sheet fully fragments into dispersed interfacial structures. Then, the intermediate Weber number of 110 is picked as the reference case to study the variation of density and viscosity between the phases separately. First, we only varied the density ratio ( $r = \rho_1/\rho_2$ ) and evaluated two cases with  $r = 0.1$  and 10. Note that the density contrast will induce differences in inertia between the phases and could alter the homogeneity assumption of the HIT flows. It also changes the kinematic viscosity and could vary the turbulence intensity. Notwithstanding these limitations, we still analyzed these cases but intentionally kept the density ratio low to minimize such effects. Finally, we varied the viscosity ratio ( $m = \mu_1/\mu_2$ ) and considered two cases with  $m = 0.1$  and 0.001. It has to be noted for the aforementioned reasons, in this study we only intended for  $m \leq 1$  because a test simulation (not presented here) disclosed that when the viscosity of the sheet is high, it does not completely fragment and stays as a highly-deformed and corrugated bulk fluid. Table 1 presents the simulation cases with the relevant physical parameters.

The box is discretized with equidistant grids of  $\Delta = L_I/512$ . Numerical simulations were performed using the VOF solver of `interIsoFoam` within the CFD software package of OpenFOAM. This finite volume solver employs a PISO-based algorithm for pressure-velocity coupling (Weller et al., 1998) and the geometric VOF method of IsoAdvector (Roenby et al., 2016) for the interface capturing. The convective and diffusive terms in the momentum equation are discretized by employing central differencing, while the convective term in the VOF equation is discretized by using the vanLeer scheme. In the context of IsoAdvector method, a `pllc-RDF` scheme is employed for the reconstruction of the interface from discretized  $\alpha$  (Scheufler and Roenby, 2019; Gamet et al., 2020). We use adaptive time stepping to advance the solution in time with a first-order Euler scheme, where the time step size is limited by a maximum Courant number corresponding to  $1/50$  of Kolmogorov time scale similar to Trontin et al. (2010). The simulations were performed until  $t/\tau_e = 22$  where  $\tau_e = 0.27$  s is the eddy turnover time based on the large scales of turbulence (Trontin et al., 2010). This is associated with the time that the kinetic energy decays to almost zero. An in-house computational cluster with 128 processors was employed in this simulation campaign. It has to be emphasized that this setup has been the subject of our previous research with multiple validation studies. To avoid repetition, we refer to Saeedipour and Schneiderbauer (2021) for more details on the simulation setup and validations.

#### 4. Results and discussions

The analysis of the simulation results is presented in three different sections based on the influences of surface tension coefficient (in the form of  $We$  number), density ratio, and viscosity ratios.

##### 4.1. Influence of the surface tension coefficient

In the first three cases, we compare the characteristics of the decaying turbulent interfacial flows with different interfacial tension between the phases. Since  $We \propto \sigma^{-1}$ , we refer to them by their Weber numbers.

Fig. 3(a) displays the normalized domain-averaged kinetic energy,  $\langle \mathcal{K} \rangle = \frac{1}{V} \int_V \frac{1}{2} \rho \|\mathbf{u}\|^2 dv$ , for the cases C-1 to C-3 together with the single-phase results. This pictures the decaying process of the present HIT flow which is globally similar for all the cases (even though we will show later the differences due to the presence of the interface). The high energy input to the box develops an inertia-dominated regime, and  $\langle \mathcal{K} \rangle$  decays monotonically with a steep rate until  $t/\tau_e \approx 6$  where it reaches the 10% of its initial value. Then, for  $t/\tau_e \geq 6$  the decay rate reduces significantly until  $t/\tau_e \approx 22$  where the remaining energy decays to almost zero, and the flow is mainly dominated by the surface tension effects. These two regimes are schematically distinguished in Fig. 3(a).

As the high-order moment of the flow, the normalized domain-averaged enstrophy,  $\langle \mathcal{E} \rangle = \frac{1}{V} \int_V \frac{1}{2} \|\nabla \times \mathbf{u}\|^2 dv$ , is plotted in Fig. 3(b). Initially, the enstrophy increases in the domain until  $t/\tau_e = 1$  which is attributed to the initialization of the HIT box and how the energy spreads to the high wavenumbers through a non-linear cascade (Yu et al., 2005). After one eddy turn-over time, the enstrophy also starts to decay with a fast rate until  $t/\tau_e \approx 6$ , then similar to the kinetic energy, it also yields a slower decay until the end of the simulation.

As the third macroscopic quantity, in Fig. 4 we plotted the domain-integrated total interfacial area  $\mathcal{A} = \int_V \delta_s dv$ , in which  $\delta_s$  is the Dirac delta function approximated by  $\|\nabla \alpha\|$  for each finite volume cell as employed in our previous works (Saeedipour et al., 2021; Saeedipour and Schneiderbauer, 2022). The temporal variation of this integral quantity is strongly coupled with  $\langle \mathcal{K} \rangle$  and  $\langle \mathcal{E} \rangle$ . The inertia-dominated regime involves strong turbulence-interface interactions leading to several corrugations and irregularities at the interface which promotes fragmentation. This results in a fast increase of the total interfacial area for each case at different times before  $t/\tau_e = 6$ . These interactions could result in more than 10 times larger interfacial area for the highest  $We$ , which is an indication of interface fragmentation and the creation of a dispersed phase. Afterward, when the energy decay rate reduces for  $6 < t/\tau_e < 22$ , the surface tension is globally dominant through the act of surface minimization and rearranging the shape of dispersed interfacial structures toward spherical droplets. Therefore, for the surface tension-dominated regime,  $\mathcal{A}$  starts to reduce and converge toward a constant value that is still larger than the initial area of the flat interface.

Furthermore, the influence of surface tension coefficient can be explained by the difference between the interfacial area profile in each case. For the C-2 with largest  $\sigma$ , the total interfacial area is much lower because of the stronger surface tension force between the phases that counteracts instabilities and interface deformation. It also leads to reaching the peak of  $\mathcal{A}$  sooner and consequently, having a globally lower interfacial area compared to other cases. In contrast, the sheet with smaller  $\sigma$  (C-3) encounters more severe deformations followed by stronger fragmentation which eventually results in a total interfacial area almost twice the C-2 at the end of simulation. This is also reflected in Fig. 5 that shows the instantaneous snapshots of the cases with  $We = 63, 110$ , and 220 for two different instants of times at  $t/\tau_e = 1$  and 6. While at the beginning of the simulations and during the inertia-dominated regime, all the cases demonstrate more or less similar patterns for interfacial structures, at the end of the simulation the case with higher  $We$  is extensively fragmented (Fig. 5(f)) whereas the case with  $We = 63$  displays a large number of spherical droplets indicating the stronger surface tension force (Fig. 5(b)). This qualitative observation indicates that the characteristic size of droplets should be larger as the Weber number decreases. Further evaluation of the characteristic length scales will be the subject of next sections.

For a better understanding of the macroscopic trends, we present a more detailed analysis concerning the differences with the interface-free case ( $We = \infty$ ). For the given turbulence in the HIT box and

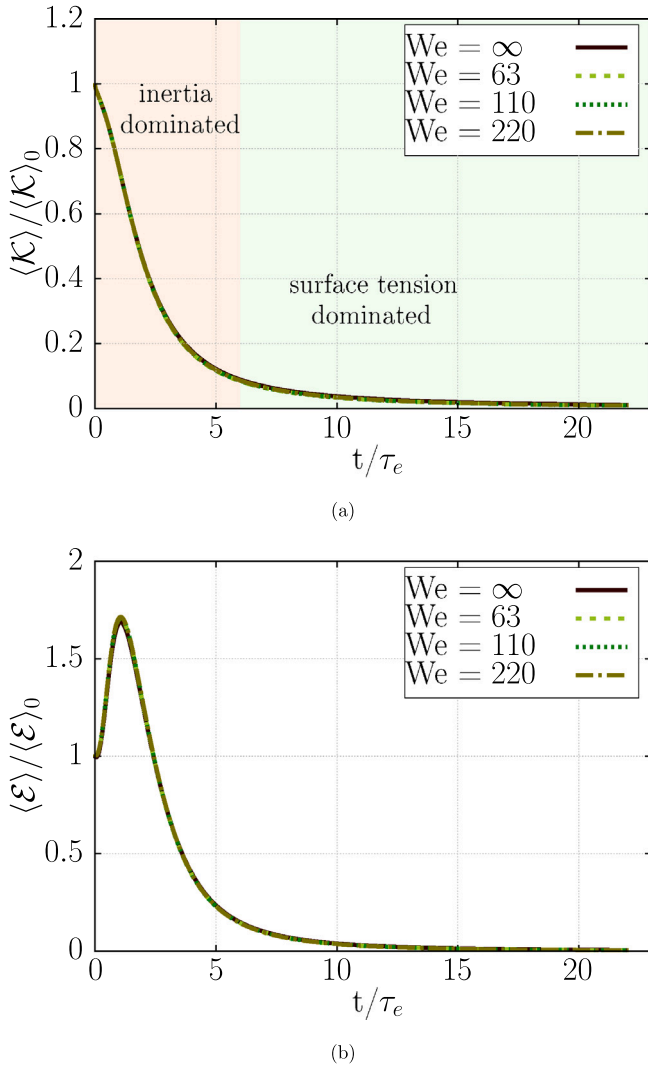


Fig. 3. Normalized domain-averaged quantities of cases C-1 to C-3 together with the single-phase HIT: (a) kinetic energy, and (b) enstrophy.

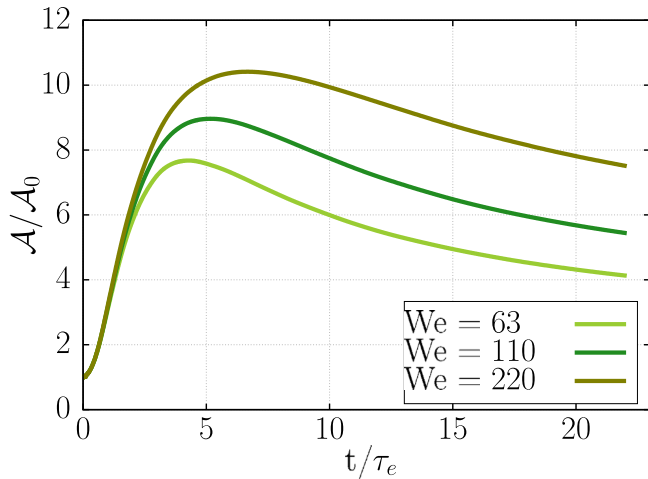


Fig. 4. Domain-integrated interfacial area for C-1 to C-3 normalized by the initial interfacial area of the flat sheet.

the absence of density and viscosity contrasts, the presence of interface globally damps the total kinetic energy compared to the interface-free

case with  $We = \infty$ . This is attributed to the amount of energy that should be consumed from the given turbulence to fragment the sheet. As also reported by Trontin et al. (2010), the temporal variation of the kinetic energy for high Weber numbers of 63 and 110 (that end up with highly fragmented droplets) remain always inferior to the single-phase TKE. This also holds for the enstrophy. Zooming into different sub-periods of Fig. 3(b) unveils that the domain-averaged enstrophy of two-phase cases is mostly lower than the single-phase one, but with different trends. During the inertia-dominated period ( $t/\tau_e < 6$ ), the lower We number consumes (damps) a greater portion of the given enstrophy to overcome stronger surface bonding during sheet fragmentation, and it has marginally the lowest enstrophy level compared to other cases as shown in Fig. 6(a). During the surface tension-dominated period; however, the trend is different and the case with the lowest Weber number yields a greater enstrophy level (Fig. 6(b)). Because in the lack of inertia, larger surface tension contributes more to enstrophy production via coalescence and surface minimization. However, it never reaches the single-phase case because for the simulated times the interface still stays dispersed. We will further analyze these interactions in spectral space and benefit from the demarcation between inertia-dominated and surface tension-dominated periods to describe the nature of turbulence–interface interactions in the present decaying HIT.

So far, the analysis of integral quantities discloses the time-dependent nature of the turbulence–interface interactions for the decaying HIT. Nevertheless, as discussed in the introduction, these interactions are also scale-dependent and the turbulent interfacial flow in the HIT box follows a cascade that results in a distribution of flow and interfacial structures across the length scales. For the remainder of our analysis, we mostly focus on the spectral analysis of the interactions. Following the discussion in sub-Section 2.3, we now analyze the contribution of different mechanisms to the enstrophy generation/destruction and assess how they characterize the dispersed interfacial flow.

For each of the cases C-1 to C-3, we compute the rates of enstrophy production/destruction by the vortex stretching ( $\Psi_{V,S}$ ) and surface tension ( $\Psi_\sigma$ ) terms in spectral space as appearing in Eq. (7). Fig. 7 displays these spectral contributions for two different times of  $t/\tau_e = 3.7$  and 11. These two instants of times are chosen to be within the inertia-dominated and surface tension-dominated regimes of the decaying HIT. The wavenumbers at which  $\Psi_{V,S} \cong \Psi_\sigma$ , corresponding to  $\kappa_c$  in Fig. 1, are also evaluated and plotted as the vertical dashed lines. For both times,  $\Psi_{V,S}$  is positive for most of wavenumbers, whereas  $\Psi_\sigma$  is negative at low wavenumbers and becomes positive at higher ones, which evidently (i) highlights the scale-dependent nature of the surface tension contribution, and (ii) explains the lower magnitudes of  $\Psi_{V,S}$  in multiphase cases compared with the single-phase one. Because the surface tension counteracts the stretching-driven cascading process for most of the large scales and decreases the rate of vortex stretching compared to the interface-free case. In fact, the surface tension misalignment term destructs the enstrophy at large scales, and thus the negative  $\Psi_\sigma$  is associated with the higher probability of fragmentation. Whereas it enhances the enstrophy at smaller scales through the act of surface minimization or when coalescence happens. Thus, the positive  $\Psi_\sigma$  indicates the probability of such enstrophy-releasing interfacial events. Fig. 7 demonstrates that larger  $\sigma$  expands the positive  $\Psi_\sigma$  toward the larger scales, which is interpreted as the dominance of coalescence over a broader range of the intermediate scales. Similarly, for the case with  $We = 220$  (i.e. lowest  $\sigma$ ) the fragmentation is stronger and the enstrophy production due to surface minimization remains limited to the highest wavenumbers which, in turn, leads to the generation of smaller droplets. It is also evident that the vortex stretching remains effective on similar range of scales but slightly diminishes as  $\sigma$  increases. This can be explained concerning the single-phase case which theoretically represents  $\sigma = 0$ , and the stronger surface tension causes a higher reduction in the vortex stretching rate as depicted in Fig. 7.

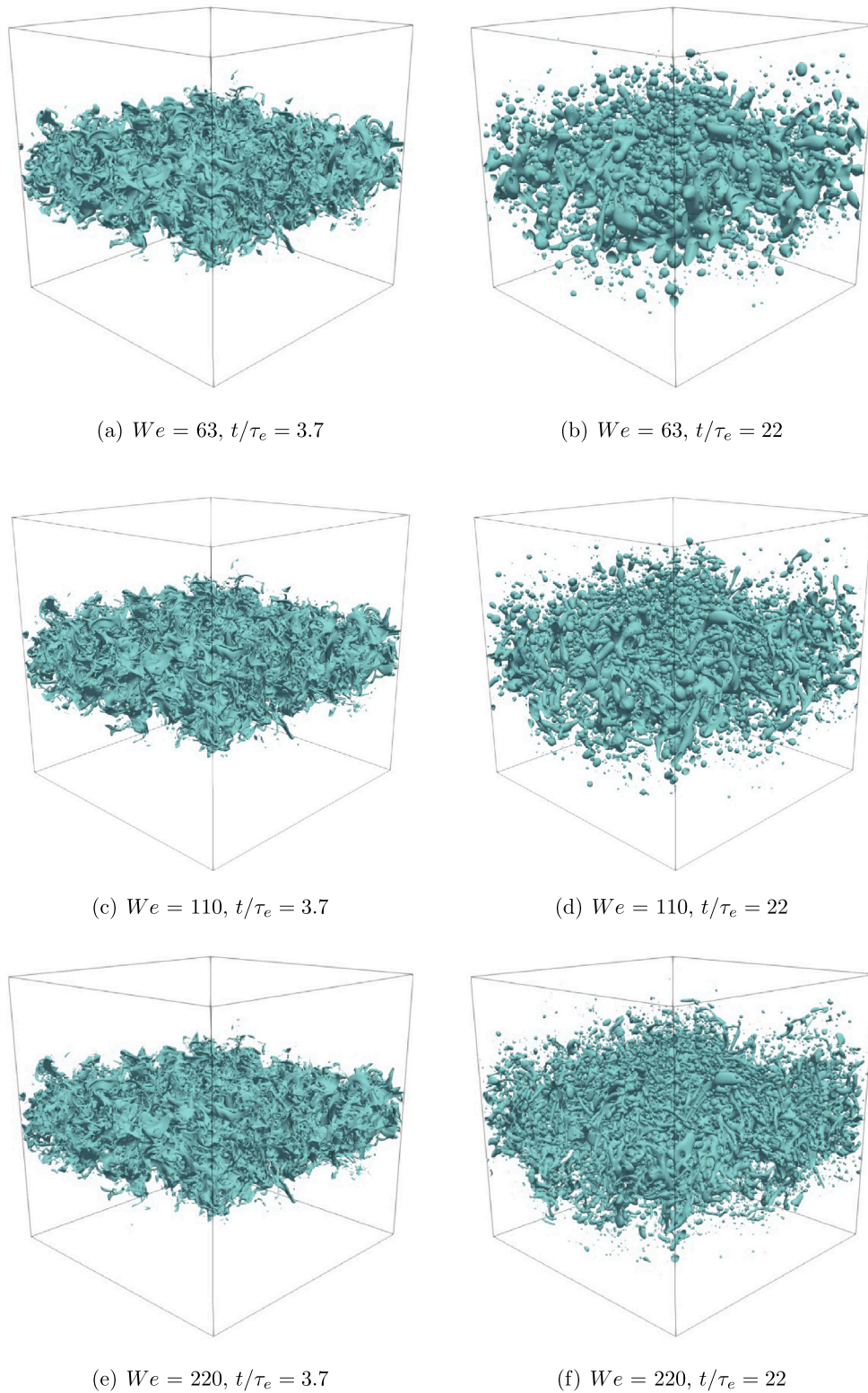


Fig. 5. Instantaneous snapshots of interfacial structures for C-1 to C-3 at different times visualized by iso-surfaces of  $\alpha = 0.5$ .

As time elapses and the turbulence intensity decays, the interactions between the mechanisms follow the same trend but shift toward the lower wavenumbers. Also, the vortex stretching rate decreases gradually and  $\Psi_\sigma \geq 0$  for a broader range of length scales. From a physical point of view, it represents an interfacial flow with temporally-decreasing disruptive forces. Thus, the consolidating effect of surface tension, which is reflected in its positive contribution rate to the

entropy, expands toward the left of the spectra, and consequently, the breakup events become limited to the larger scales. This entails the generation of larger stable droplets at  $t/\tau_e = 11$  compared to  $t/\tau_e = 3.7$ . It has to be noted that the  $\Psi$  terms are multiplied by  $\kappa^2$  for better visibility, thus the relative trends, as well as the critical wavenumbers remain intact.

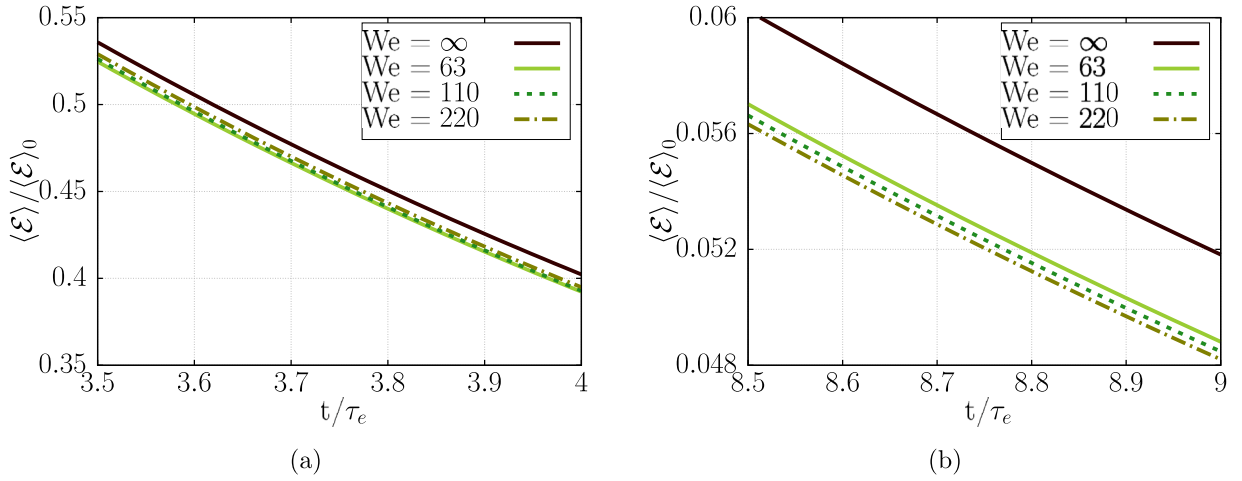


Fig. 6. Two sub-periods of the temporal variation of domain-averaged entropy: (a) inertia-dominated, and (b) surface tension-dominated regimes.

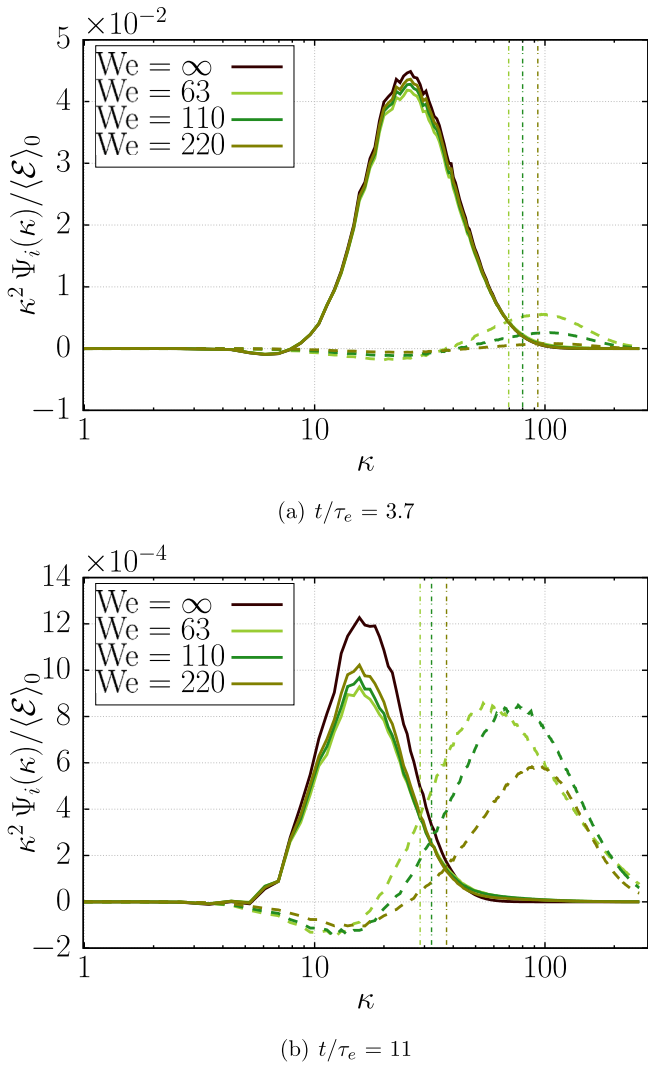


Fig. 7. The spectral rate of entropy transport by the vortex stretching term  $\Psi_{VS}$  (solid curves) and surface tension term  $\Psi_\sigma$  (dashed curves) for cases C-1 to C-3 at two instants of time. The values are normalized by the initial domain-averaged entropy and multiplied by  $\kappa^2$  for better visibility. The vertical dash-dotted lines indicate  $\kappa_c$  for the case with the same color. (For interpretation of the references to color in this figure legend, the reader is referred to the web version of this article.)

As the main characteristic scales explained in sub-Section 2.3, we track both  $\kappa_c$  and  $\kappa_s$  (associated with  $\Psi_\sigma \cong 0$ ) with time. Fig. 8 presents a comparison of these two wavenumbers during the simulation for all the three cases. Their temporal variation is in accordance with the aforementioned physical description: they decrease with time, and for the higher  $We$ , they yield larger values. As discussed earlier, these two characteristic wavenumbers could represent a range for maximum stable droplets. Fig. 8 reveals that at the initial stages of the HIT, the  $|\kappa_c - \kappa_s|$  is very large, and as the turbulence intensity decreases with time, they converge.

For better physical understanding of this range, it would be instructive to imagine a vortical structure (eddy) corresponding to an arbitrary wavenumber between  $\kappa_s$  and  $\kappa_c$  which is transported within an interfacial structure (droplet) of the same size. On the one hand,  $\Psi_\sigma$  is positive, and therefore the act of surface minimization (that resists droplet deformation) produces vorticity. On the other hand, still  $\Psi_{VS} > \Psi_\sigma$ , and the eddy is being stretched, locally increases vorticity, and counteracts surface tension. It infers that a critical range of wavenumbers exists (i.e.  $\kappa_s < \kappa < \kappa_c$ ) for which turbulent eddies may still be able to deform and break the interfacial structures. As the turbulence decays and the vortex stretching mechanism becomes globally lower, this critical range becomes smaller until almost vanishes. Whereas for  $\kappa > \kappa_c$  (above the solid curves in Fig. 8), the vortex stretching is always weaker than the rate of surface tension contribution, and the droplets are physically stable. It makes  $\kappa_c$  a more plausible candidate to define the Hinze scale with. Particularly, for non-decaying turbulence which is more or less similar to the initial stages of decaying HIT, the large  $|\kappa_c - \kappa_s|$  points out the probability of wide range of critically-stable droplets.

To further explore the scale-dependent nature of interactions, we analyze the turbulent energy spectrum and the role of the characteristic length scales. To compute the energy spectra in isotropic turbulence, we follow the mathematical formulation of the one-dimensional spectrum (Tennekes and Lumley, 1972; McComb, 1992) by averaging the Fourier transform of correlation tensor  $Q_{ii}$  over a series of spherical shells of radius  $\kappa$  i.e.  $\frac{1}{2} \oint Q_{ii}(\kappa) da$  for a spherical shell with the area of  $da$ . Therefore, the final form of energy spectrum is computed by summing up over all the wavenumbers and reads

$$E(\kappa) = \frac{1}{2} \sum_{\kappa < |\mathbf{k}| < \kappa+1} \hat{\mathbf{u}}(\mathbf{k}, t) \circ \hat{\mathbf{u}}(\mathbf{k}, t), \quad (10)$$

where the complex dot product is actually conducted by employing the complex conjugate of the  $\hat{\mathbf{u}}(\mathbf{k}, t)$  in our post-processing algorithm.

Fig. 9 displays the energy spectra for each interfacial HIT in cases C-1 to C-3 together with single-phase spectra at the same time. It is evident that the energy cascade of all the interfacial HITs deviates from

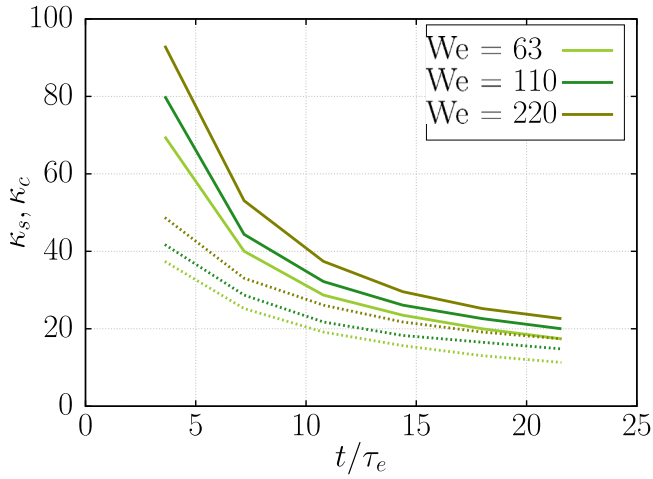
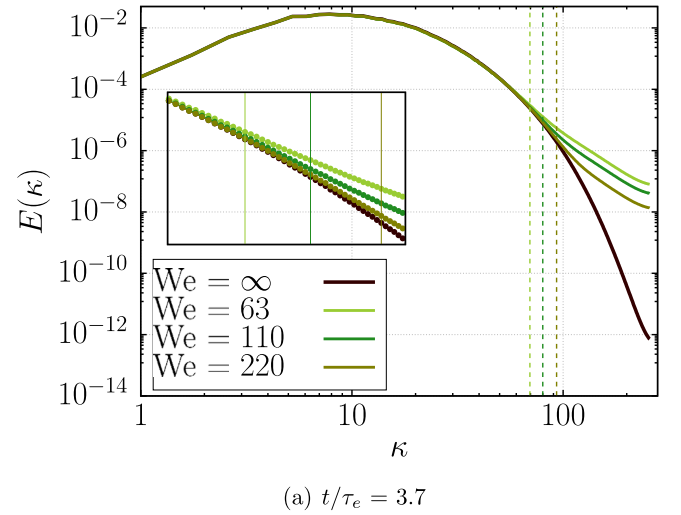


Fig. 8. Temporal variation of the characteristic wavenumbers  $\kappa_c$  (solid lines), and  $\kappa_s$  (dotted lines) for cases C-1 to C-3.

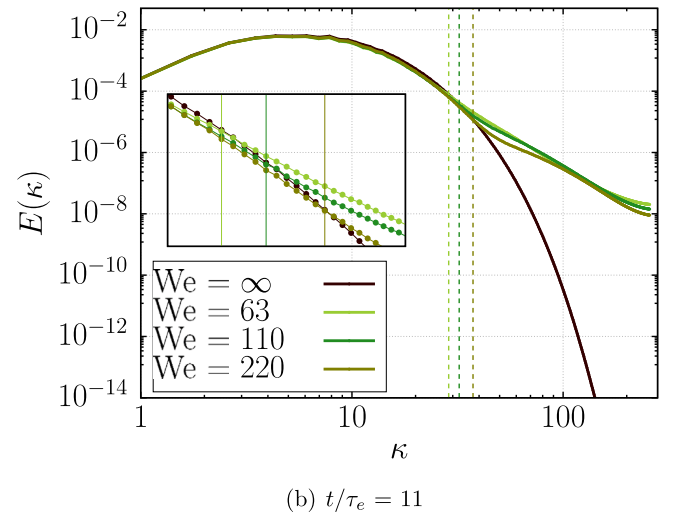
the single-phase one at large wave numbers. As described before, by increasing the surface tension coefficient, this deviation point shifts to the smaller wavenumbers which is similar to the trend of  $\Psi_\sigma$  in Fig. 7. Moreover, the energy levels after the deviation increase with the surface tension coefficient. In fact, for the C-2 (with the largest  $\sigma$ ), the energy levels at small scales become the largest. This clearly underlines the higher amount of energy production due to surface minimization and/or coalescence at the small scales for the case with stronger surface tension. Similar to  $\Psi_\sigma$ , this description holds true when turbulence decays, but the characteristic wavenumbers decrease with time. As also reported in our previous work (Saeedipour and Schneiderbauer, 2022), an identical behavior is also observed for enstrophy spectra computed similarly (i.e. by employing the Fourier transform of the vorticity vector in Eq. (10)); however, in this study to avoid repetition we only present energy spectra as the more conventional spectrum in the context.

As an essential observation, it is evident that the deviations in cascades occur at the same wavenumbers corresponding to  $\kappa_c$  that are also plotted in Fig. 9. As evidently exhibited by inset plots,  $\kappa_c$  acts as a transition border between the wavenumbers whose energy content is lower than the single-phase spectrum, and those with higher energy. It should be noted that the present configuration with the thin sheet as the initial condition is subject to non-homogeneity in the direction perpendicular to the sheet, and the energy spectra vary along with the  $y$ -direction as the interface propagates (Trontin et al., 2010). While the described correlation between enstrophy rates and energy spectra remains the same in all the distances from the center of the box, this could pose questions on the exact values of the characteristic length scales. The potential issues with such an initial condition for interfacial HIT require a more detailed discussion, which will be provided later in the conclusions.

It remains to find the footprint of  $\kappa_c$  in statistical quantities of interfacial structures across the length scales and confirm its relevance to defining the Hinze scale. A reasonable approach would be similar to Cialesi-Esposito et al. (2023) which analyzes the size distribution of droplets and demonstrate how scaling laws change across the PDF of droplet sizes generated during the emulsion of droplets in a non-decaying HIT. They observe the change in the slopes from  $-3/2$  to  $-10/3$  around the estimated Hinze scale. However, this observation may be difficult to make for all the HIT flows. A recent investigation by Begemann et al. (2022) reports such limitation for emulsification in non-decaying HIT. While they could observe the  $-3/2$  slope of the small-scale droplets in their different cases, the sharper slope of  $-10/3$  was not generally discernible for multiple ones. It would be even more difficult for the present unsteady decaying HIT. The global picture



(a)  $t/\tau_e = 3.7$



(b)  $t/\tau_e = 11$

Fig. 9. The kinetic energy spectra of cases C-1 to C-3 as well as the single-phase HIT at different instants of time: (a)  $t/\tau_e = 3.7$ , and (b)  $t/\tau_e = 11$ . The vertical dashed lines indicate  $\kappa_c$  for the case with the same color. The inset plots zoom in around the deviation ranges in spectra compared to the single-phase problem. (For interpretation of the references to color in this figure legend, the reader is referred to the web version of this article.)

of the interfacial structures (including e.g. several highly-corrugated ligaments) at the early stages of the problem challenges the reach of a meaningful statistical analysis of the droplet sizes, as also evident from the snapshots on the left column of Fig. 5. Besides, even after the interfacial structures become more dispersed, a fragmentation cascade with the reported scaling laws may not form as the HIT decays continuously.

Given these limitations, we compute the instantaneous droplet size distribution using the connected-component labeling concept. For each instant of time, this approach searches through the entire 3D domain and detects individual isolated interfacial structures based on the connected cells containing a threshold of volume fraction field. By assigning an equivalent droplet diameter to each of them, the detected structures are grouped in bins with a width equal to the grid size. A cut-off size of  $d/\Delta = 3$  is also applied to remove the uncertainty of detecting non-physical droplets. This method is implemented as an OpenFOAM-based post-processing tool that we have used in our previous works (for more details we refer to Saeedipour and Schneiderbauer (2021)). Fig. 10 displays the PDF of droplets for each case at  $t/\tau_e = 11$  (where the droplets become dispersed). To be consistent with the previous plots, the horizontal axis is shown by  $2\pi/d$  which presents an equivalent

wavenumber based on the droplet sizes. This allows plotting  $\kappa_c$  for better comparison in each case. Two straight lines are fitted to the data in each plot with positive slopes. It is evident that in all the cases, the size distribution follows these straight lines and changes the slope at a length scale associated with  $\kappa_c$ . Even though these slopes are not similar to that reported for non-decaying HIT (i.e. they are case-dependent and vary between 2.8 to 3.6 for the red ones, and 6.6 to 7.3 for the blue ones), the distinct change in the slopes from the gentler to the sharper one is aligned with the definition of the Hinze scale where a change in the interfacial breakup mechanisms occurs. In other words, these instantaneous distributions of the droplets reveal a change in fragmentation cascade and distinguish between stable droplets and structures that are prone to break up.

In addition to the droplet size distributions, we investigate another spectral quantity that could represent the statistics of interfacial structures. Inspired by a recent experimental study on the fragmentation of gas–liquid flow (Zhang and Chanson, 2019), we compute the power spectrum of the volume fraction scalar field. Similar to the energy spectrum, we follow the spherical-shell integration strategy, and since in isotropic turbulence the auto-correlation function depends only on the wavenumber (Tennekes and Lumley, 1972), the wavenumber spectrum of the volume fraction field is computed by

$$P_\alpha(\kappa) = \sum_{\kappa < |\kappa| < \kappa+1} \mathcal{R} \left\{ \hat{\alpha}^*(\kappa, t) \cdot \hat{\alpha}(\kappa, t) \right\}, \quad (11)$$

where  $\mathcal{R}\{\}$  represents the real part of the complex field and “ $*$ ” denotes the complex conjugate of the Fourier transform.

Fig. 11 presents the wavenumber spectrum of volume fraction for the cases C-1 to C-3. For all the cases the  $P_\alpha(\kappa)$  is almost flat or may increase at small and intermediate wavenumbers, and starts to decay at certain high wavenumbers. The decay rate reveals a tendency toward  $\kappa^{-2}$  slope that is consistent with the observations in previous works (McCaslin and Desjardins, 2014; Zhang and Chanson, 2019). In an analogy with the turbulent energy cascade where the presence of viscous effects imposes a sharp decay at small scale fluctuations, the decay in  $P_\alpha(\kappa)$  would physically correspond to the presence of a suppressing mechanism against interface fluctuations i.e. deformations. In other words, for the wavenumbers at which the  $P_\alpha(\kappa)$  decays, the surface tension becomes dominant. It suppresses those interface corrugations that could have led to droplet breakup, and prevents enstrophy consumption due to severe deformations and breakup events. This interpretation is aligned with the explanation of McCaslin and Desjardins (2014) for the role of surface tension in spectral space. Fig. 11 further displays the characteristic wavenumbers plotted by vertical lines. For almost all the cases,  $\kappa_c$  lies at the beginning of the decay with the  $\kappa^{-2}$  slope, even though the decay rate may increase at larger wavenumbers. This is more evident at later time as a more dispersed droplet-laden flow is formed. Moreover, as the surface tension coefficient increases, the decay starts at larger scales. Similar to the trend of  $\Psi_\sigma$ , as turbulence decays, the surface tension suppresses a wider range of interface fluctuations and  $P_\alpha(\kappa)$  starts to decay at lower wavenumbers (Fig. 11(b)).

These two observations on the size distribution and volume fraction spectra clearly connect the enstrophy transport to the statistics of interfacial structures and confirms the role of  $\kappa_c$  in shaping the scale-dependent trends in interfacial turbulence. Thus, in the remainder of the analysis, we will mostly focus on this characteristic length scale and evaluate how it varies with different parameters. Also, as the applicability of the volume fraction spectrum may be limited for every interfacial flow, for the next cases we only present the size distribution of the droplets as the relevant statistical representation of the dispersed flow.

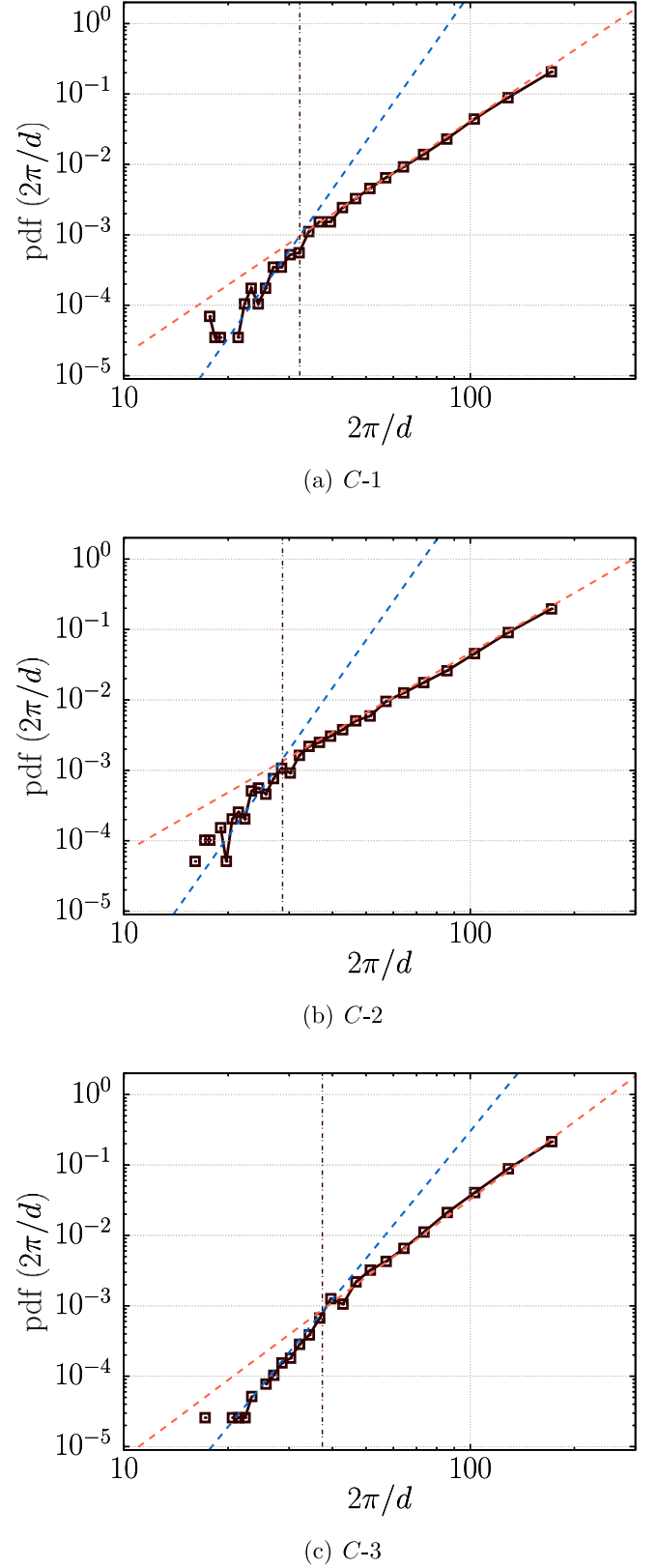
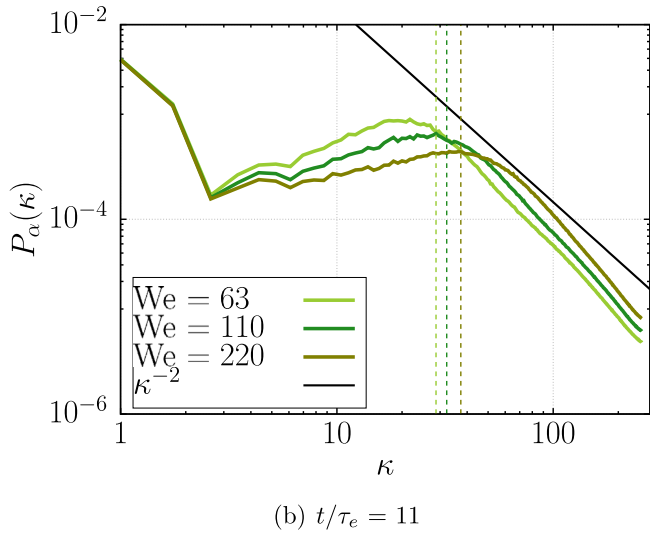
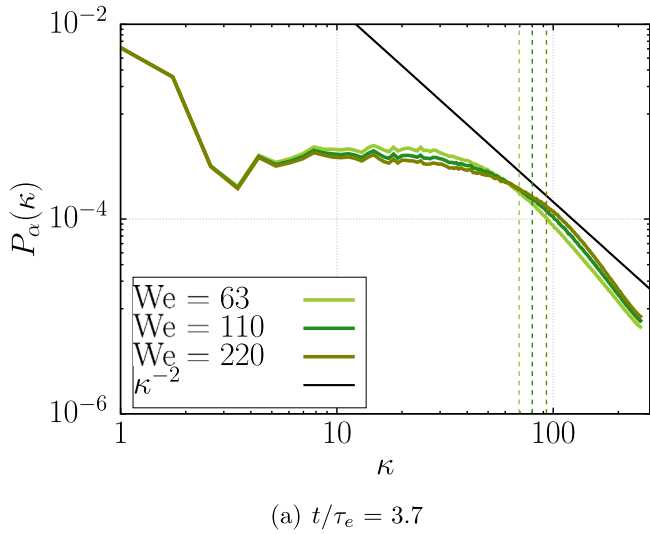


Fig. 10. Size distribution of droplets at  $t/\tau_c = 11$  for different cases: (a) C-1, (b) C-2, and (c) C-3. The vertical dash-dotted lines show the computed  $\kappa_c$  for each case. The blue and red dashed lines are fitted to track the change in the PDF slope. (For interpretation of the references to color in this figure legend, the reader is referred to the web version of this article.)



**Fig. 11.** The wavenumber spectra of the volume fraction scalar field for C-1 to C-3 at different instants of time: (a)  $t/\tau_e = 3.7$ , and (b)  $t/\tau_e = 11$ . The vertical dashed lines indicate  $\kappa_c$  for the case with the same color. (For interpretation of the references to color in this figure legend, the reader is referred to the web version of this article.)

#### 4.2. Influence of the density contrast

The density contrast between the phases influences both temporal and spectral characteristics of turbulence–interface interactions. Fig. 12(a) presents the temporal variation of domain-averaged enstrophy for the cases C-4 and C-5 together with the reference case of C-1. Total domain-averaged enstrophy increases with the density of the sheet, as the inertial effects in the system intensify vorticity production at the beginning of the HIT. The decay rate is also more abrupt for the case with the higher density. This enhancement is not limited to enstrophy and the total interfacial area is also affected. Fig. 12(b) displays the temporal evolution of  $\mathcal{A}$  for the cases C-1, C-4, and C-5. For  $r = 10$ , the sheet is subject to the highest degree of fragmentation between the investigated cases in this study and grows abruptly to 15 times the initial value during the inertia-dominated period of the decaying HIT (i.e.  $t/\tau_e \leq 6$ ). This highlights the role of density contrasts on the interface deformation and breakup for given turbulence. By opposite, the total interfacial area remains lower than the reference case for the  $r = 0.1$ . In other words, the reduction of density ratio suppresses severe interface stretching and deformation initiated by the turbulence, and in turn, results in a lower total interfacial area.

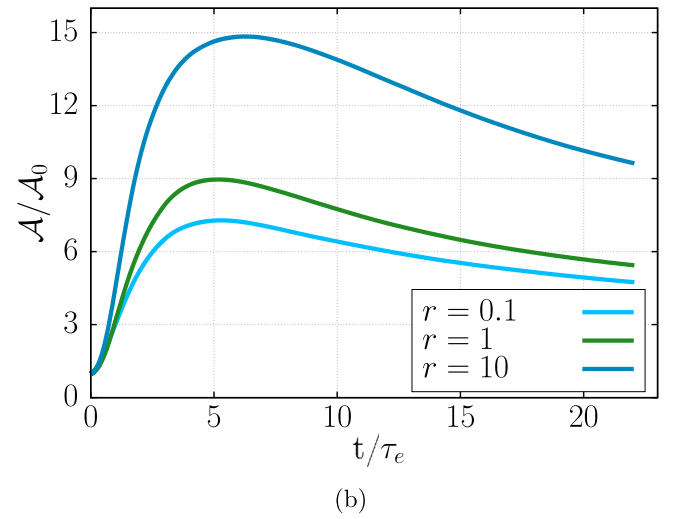
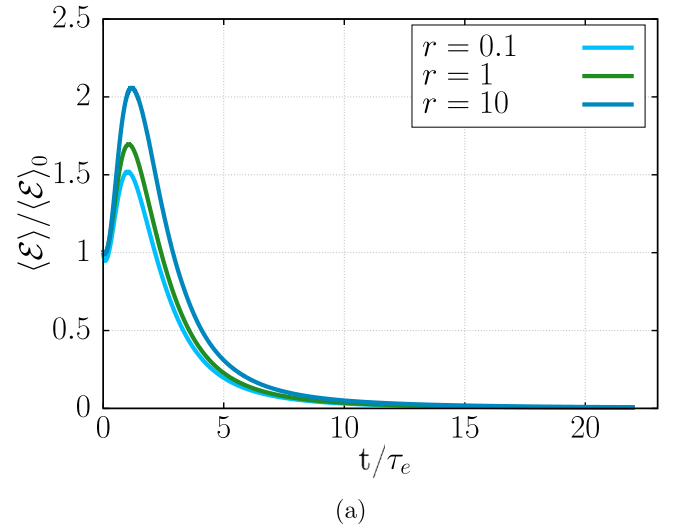


**Fig. 12.** Normalized domain-averaged quantities of cases C-4 and C-5 together with the reference case C-1: (a) enstrophy, and (b) total interfacial area.

This trend is consistent with the recent findings of Mangani et al. (2022) where the reduction of density ratio decreases the probability of bearing high curvature during the interface deformation.

Fig. 13 compares instantaneous snapshots of the interfacial structures at  $t/\tau_e = 3.7$  and 11 for the cases C-4 and C-5. It confirms that the initial energy transfer to the sheet for  $r = 10$  results in a fragmented regime that remains highly dispersed until the last simulated time ( $t/\tau_e = 22$ ). Therefore, it yields a much higher interfacial area than the reference case. Similarly, for  $r = 0.1$ , the surface tension-dominated period shrinks the total interfacial area and results in a dispersed flow with many smooth interfacial structures as visualized in Fig. 13(b).

We further evaluate the turbulence–interface interactions in spectral space. Fig. 14 presents the rate of enstrophy generation/destruction by the vortex stretching and surface tension misalignment terms. It is evident that increasing  $r$  enhances  $\Psi_{VS}$  and dilates its spectral distribution to a wider range of small scales. This higher inertia, for instance in the case of C-5, keeps the surface tension rate negative for a wider range of scales and restricts the positive  $\Psi_\sigma$  within a short range of high wavenumber motions. Therefore,  $\Psi_\sigma \cong \Psi_{VS}$  occurs at much higher wavenumbers compared to C-4 and C-1; however, the surface tension rate never exceeds the vortex stretching one as depicted in Fig. 14(a). This infers a critical condition where the droplets may still be unstable, or end up with sub-Kolmogorov droplets. However, further analysis

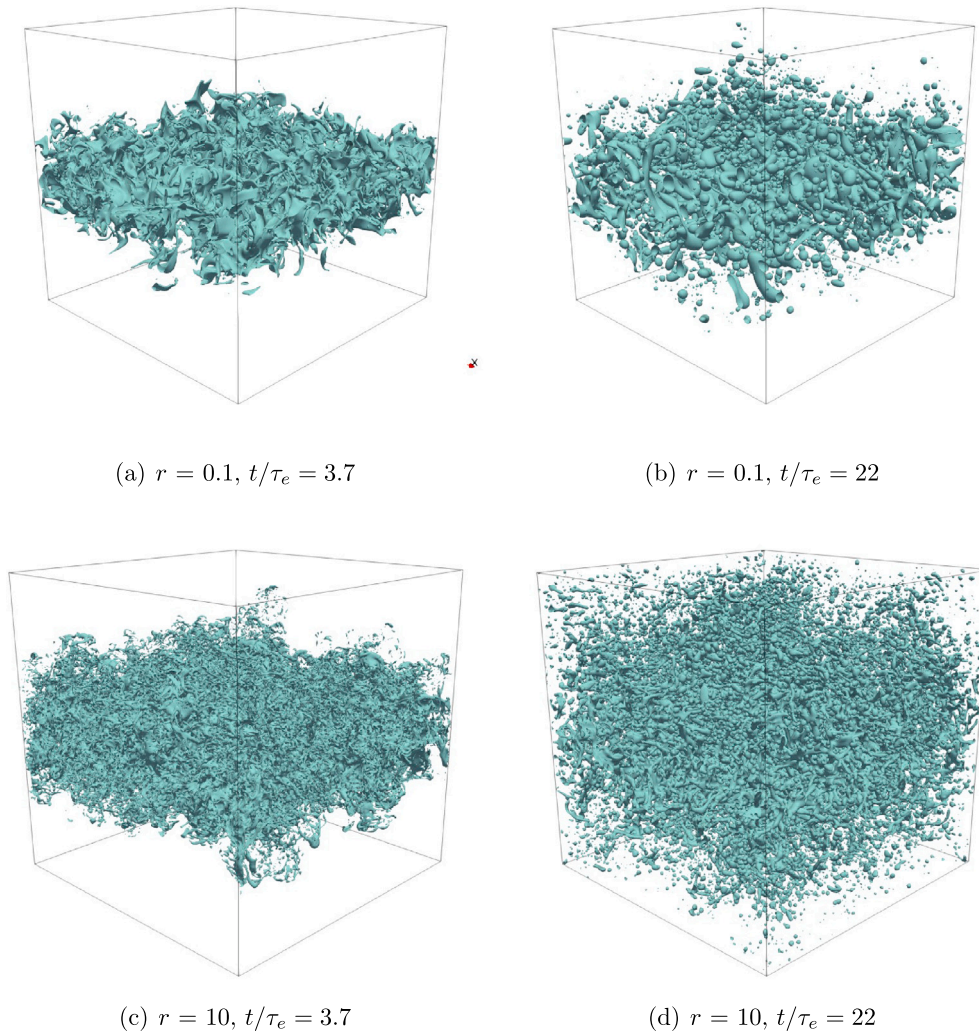


Fig. 13. Instantaneous snapshots of interfacial structures for C-4 (top row) and C-5 (bottom row) at different times visualized by iso-surfaces of  $\alpha = 0.5$ .

in this direction requires a more detailed statistical analysis on the droplets that may be difficult for the present highly-unsteady decaying HIT and therefore remains for future study. Decreasing density ratio shifts the competition between vortex stretching and surface tension in the opposite direction, and involves larger scales. As evident for C-4 with density ratio of 0.1,  $\Psi_\sigma \geq 0$  for a wider range of spatial scales and this, in turn, implies a lower probability of fragmentation in entire spectral domain. This interpretation evidently explains the appearance of large-scale corrugated structures at the early stages of C-4 and the massive generation of small droplets in C-5 at the same time, as demonstrated in Fig. 13(a) and (c).

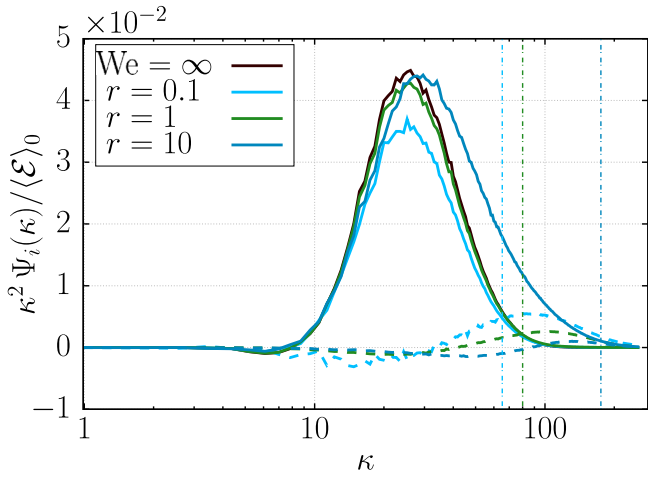
Over time, the vortex stretching rate gradually diminishes while  $\Psi_\sigma$  grows for all the cases, and both mechanisms extend their scope of impact toward the larger scales. Particularly for  $\Psi_\sigma$ , this situation leads to lower  $\kappa_c$  as shown in Fig. 14(b). As the most determinative role of the density ratio in this entrophy-based analysis it could be concluded that by increasing  $r$ , the vortex stretching mechanism is enhanced and broadened toward the smaller scales, while decreasing  $r$  amplifies the positive  $\Psi_\sigma$ , and further extends it toward the larger scales. Therefore, it can be interpreted that higher  $r$  facilitates fragmentation, and lower  $r$  enhances coalescence and surface minimization. This conclusion is also confirmed by a comparison of the characteristic length scales. Fig. 15 displays the temporal variation of the characteristic wavenumbers for cases C-1, C-4, and C-5. While  $\kappa_c$  and  $\kappa_s$  decrease with time as expected, the case with the higher density ratio has the maximum  $\kappa_c$ , which indicates that the stable droplets are much smaller than other

two cases. The large difference between these two wavenumbers is also maximum for the  $r = 10$ , indicating a potential large range of critically-stable droplets.

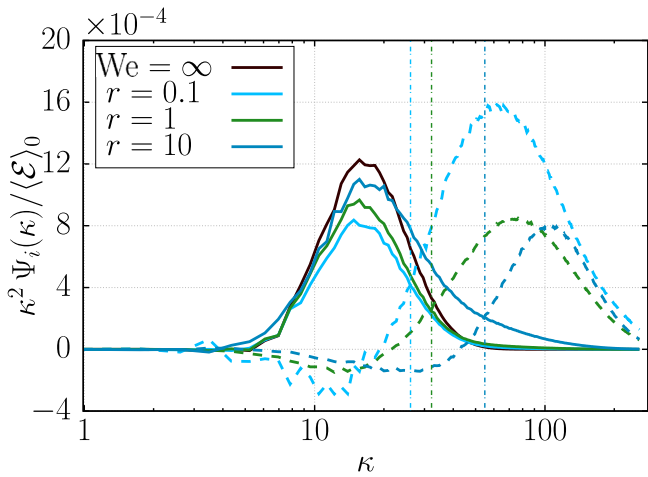
Finally, the size distribution of the droplets at  $t/\tau_e = 11$  for each case is presented in Fig. 16. Similar to the previous PDF plots, straight lines with positive slopes are fitted to each curve. It reveals that the change in the slope toward a sharper one occurs at  $\kappa_c$ . Even though the change is not as evident as Fig. 10, the difference in trends due to the density ratio is evidently pictured. As the density ratio increases, the probability of smaller droplets increases and change in the slope of the PDF shifts toward the smaller droplets confirming that a larger number of droplets are prone to break up due to the higher inertia in the flow.

#### 4.3. Influence of the viscosity contrast

It remains to investigate the influence of the viscosity ratio on the temporal and spectral quantities. The domain-averaged entrophy for the cases with different viscosity ratios is plotted in Fig. 17(a). It shows that decreasing the viscosity ratio (lowering the sheet viscosity) produces more entrophy. Because this entails a globally lower resistance against the evolution of turbulence during the initialization of the HIT flow. However, for such a low volume fraction of the sheet, further decreasing the viscosity could only marginally increase the entrophy generation. This is evident in a comparison of  $\langle \mathcal{E} \rangle$  in cases C-6 and C-7.



(a)  $t/\tau_e = 3.7$



(b)  $t/\tau_e = 11$

**Fig. 14.** The spectral rate of entrophy transport by the vortex stretching term  $\Psi_{V,S}$  (solid curves) and surface tension term  $\Psi_\sigma$  (dashed curves) for cases C-4 and C-5 together with C-1 at two instants of time. The values are normalized by the initial domain-averaged entrophy and multiplied by  $\kappa^2$  for better visibility. The vertical dash-dotted lines indicate  $\kappa_c$  for the case with the same color. The black solid curves show the single-phase results for better comparison. (For interpretation of the references to color in this figure legend, the reader is referred to the web version of this article.)

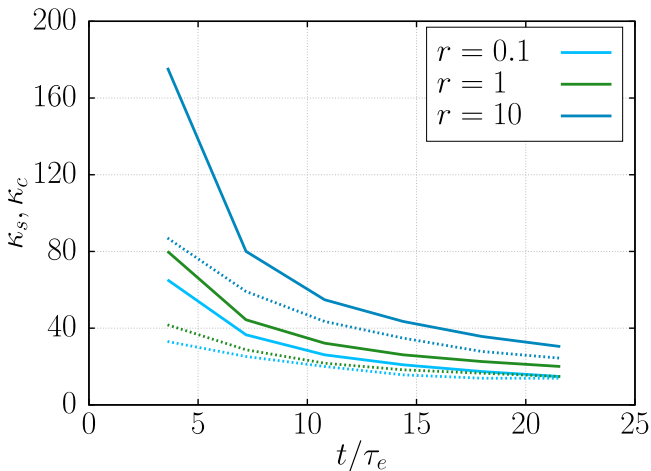
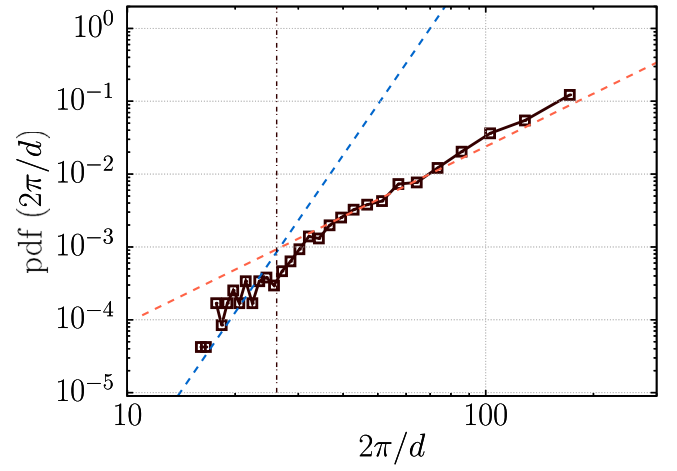
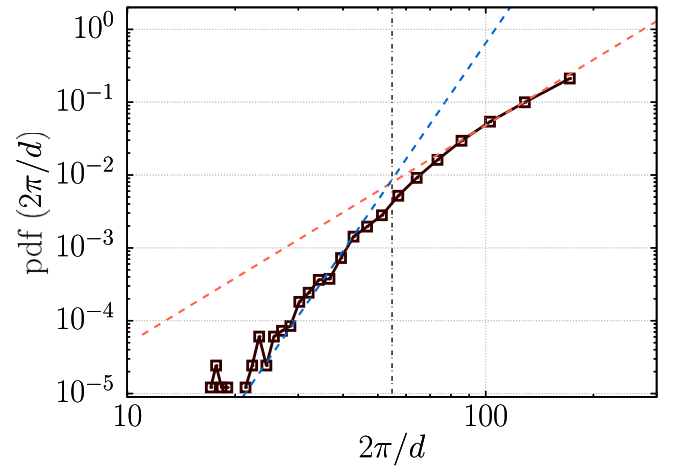


**Fig. 15.** Temporal variation of the characteristic wavenumbers  $\kappa_c$  (solid lines), and  $\kappa_s$  (dotted lines) for cases C-4 and C-5 together with the reference case of C-1.



(a) C-4



(b) C-5

**Fig. 16.** Size distribution of droplets at  $t/\tau_e = 11$  for different cases: (a) C-4 and (b) C-5. The vertical dash-dotted lines show the computed  $\kappa_c$  for each case. The blue and red dashed lines are fitted to track the change in the PDF slope. (For interpretation of the references to color in this figure legend, the reader is referred to the web version of this article.)

In addition, the viscosity variation also influences the total interfacial area. Fig. 17(b) presents the temporal evolution of  $\mathcal{A}$  for cases C-6 and C-7 as well as the reference case of C-1. During the inertia-dominated regime of the decaying HIT, lower viscosity facilitates the deformation of the sheet and enhances fragmentation. This consequently results in a higher interfacial area compared to the reference case. Similar to entrophy, further decreasing the sheet viscosity confirms the trend, but seems to have a marginal effect on this integral quantity because of the low volume fraction of 5%. As the HIT decays and during the surface tension-dominated regime (for  $t/\tau_e \geq 6$ ), the total interfacial area decreases and becomes even lower than the reference case with  $m = 1$ . Because in the absence of inertia, the fate of the dispersed regime is controlled by the viscous and surface tension forces (reminding the concept of Capillary number). Therefore, at equal density and surface tension coefficient, the lower viscosity leads to a stronger consolidating impact of the surface tension, which results in further surface minimization, and promotes coalescence. The latter decreases the number of droplets and eventually results in a lower interfacial area. Fig. 18 displays snapshots of the dispersed phases for C-7 at the end of the simulation. A qualitative comparison with

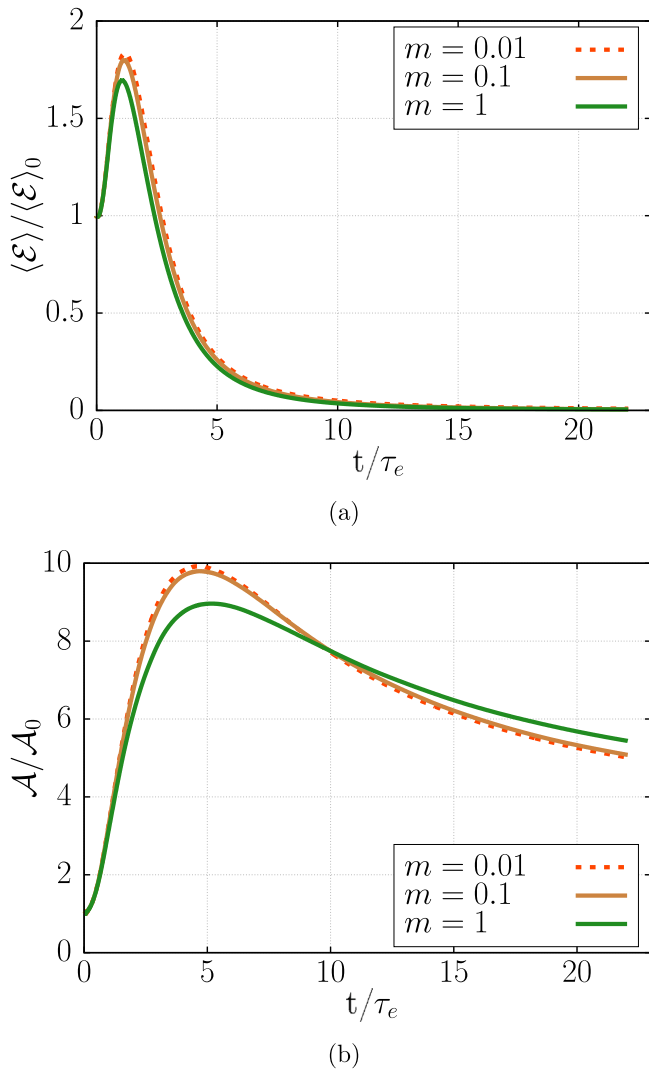


Fig. 17. Normalized domain-averaged quantities of cases C-6 and C-7 together with the reference case C-1: (a) enstrophy, and (b) total interfacial area.

Fig. 5(c)–(d) confirms the generation finer structures at  $t/\tau_e = 3.7$  and more spherical ones at  $t/\tau_e = 22$  due to the higher coalescence rate. This explanation is also consistent with Dodd and Ferrante (2016) who assessed the rate of coalescence in decaying HIT with viscosity ratio.

Similar to other parameters, the influence of viscosity contrast can be more elaborated in spectral space. Fig. 19 presents the rate of enstrophy transport by the vortex stretching and surface tension mechanisms for cases C-1, C-6, and C-7 at two instants of time. At  $t/\tau_e = 3.7$ , lower viscosity ratio increases  $\Psi_{VS}$  and extends its influence to higher wavenumbers compared to the reference case. It underlines a basic fact in the physics of turbulence: the lower the viscous effects are the stronger the vortex stretching becomes. Therefore, the vortex could uphold the stretching–pinching events for much smaller eddies. Therefore, similarly to what we observed with increasing the density ratio, lowering  $m$  promotes fragmentation by expanding negative  $\Psi_\sigma$  territory toward the higher wavenumbers, and limiting positive  $\Psi_\sigma$  to a much shorter range compared to the reference case. Consequently, both  $\kappa_c$  and  $\kappa_s$  increase as viscosity decreases.

As time elapses, the nature of interactions remains the same but shifts to the lower wavenumbers as shown in Fig. 19(b). The vortex stretching is effective on the intermediate scales and becomes slightly higher for lower viscosity ratios. Also, the difference between  $m = 0.1$  and  $0.01$  diminishes over time and their  $\Psi_\sigma$  profiles more or less

converge and reveal similar characteristic wavenumbers. Nevertheless, at small scales, the maximum  $\Psi_\sigma$  is still greater for  $m = 0.01$ . This evidently confirms the higher rate of coalescence for smaller droplets at lower viscosity which is also reflected in the total interfacial area (in Fig. 17(b)).

Fig. 20 demonstrates the temporal variation of  $\kappa_c$  and  $\kappa_s$ . These characteristic wavenumbers increase by lowering the viscosity. Nevertheless, as the surface tension coefficient is equal for all three cases, at the end of the decay the size of the maximum stable droplets converges to a similar value, and for the lowest viscosity ratio, the maximum size could be even larger than the reference case C-1 because of the enhanced coalescence rate. This is also consistent with the results of Dodd and Ferrante (2016) for the end of decaying HIT.

For the sake of completeness, we also present the statistics of interfacial structures. Fig. 21 presents the size distribution of the droplets at  $t/\tau_e = 11$  for cases C-6 and C-7. As expected, both PDF profiles show a very similar trend and the change in the slope occurs at the same scale for both cases. This is consistent with the overall picture of the viscosity difference in the current study and similar  $\kappa_c$  for both cases most of the time.

#### 4.4. Approximation of the Hinze scale from the simulations

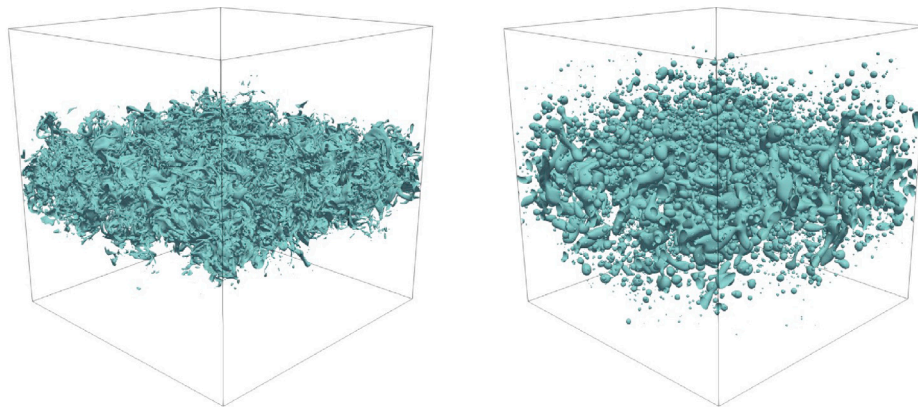
The reliance of the Hinze scale correlation on adjustable constant parameters motivates further derivations toward a more general form for the size of maximum stable droplets. The findings of the present analysis underline the role of two characteristic wavenumbers  $\kappa_c$  and  $\kappa_s$  in describing the trends of physical interactions in interfacial turbulence, and as mentioned in sub-Section 2.3, we believe  $\kappa_c$  could serve as the basis for development. We start with the physical definition of the stable droplet in turbulence, we follow the approach suggested by McCaslin and Desjardins (2014) assuming the simple idea that surface tension resists the deformations induced by turbulence eddies. If the surface tension is sufficiently strong, the eddy of size  $\mathcal{L}$  with characteristic velocity scale of  $u_\mathcal{L}$  stops overturning the interface, and an energy balance could be established between surface tension and inertia, which reads

$$\rho u_\mathcal{L}^2 \mathcal{L}^3 \approx \sigma \mathcal{L}^2. \tag{12}$$

This energy balance reminisces the concept of the critical Weber number of unity, which is applicable in the context of droplet breakup. But an estimate of  $\mathcal{L}$  is sensitive to the choice  $u_\mathcal{L}$ , which in turn depends on where this characteristic length scale falls within the universal equilibrium range (McCaslin and Desjardins, 2014). For the eddy within the inertial sub-range of turbulence,  $u_\mathcal{L} \sim (\epsilon \mathcal{L})^{1/3}$ , and for the dissipation range  $u_\mathcal{L} \sim (\epsilon \nu)^{1/4}$ , where  $\epsilon$  and  $\nu$  are the dissipation rate and kinematic viscosity, respectively (Pope, 2000). Employing the former into Eq. (12) results in a length scale proportional to  $\epsilon^{-2/5}$ , as appears in Eq. (8). Nevertheless, the trend of characteristic length scales in this study suggests that the stable droplet should be larger than the Kolmogorov length scale, but not too large to lie within the inertial sub-range. In addition, for such a decaying HIT configuration with relatively low Reynolds number, the inertial sub-range may not form. Therefore, we employ a velocity scale associated to the Taylor microscale ( $\lambda$ ) which is  $u^2 = \epsilon \lambda^2 / 15 \nu$  (Pope, 2000). This scale is pertinent in the context of atomization and has been adopted before to describe droplet formation by turbulent eddies (Saeedipour et al., 2016). By assuming  $\mathcal{L} \sim \lambda$  and rearranging Eq. (12), the characteristic length scale for the largest stable droplets reads

$$\mathcal{L} = \left( \frac{15 \sigma \nu}{\rho} \right)^{1/3} \epsilon^{-1/3} \tag{13}$$

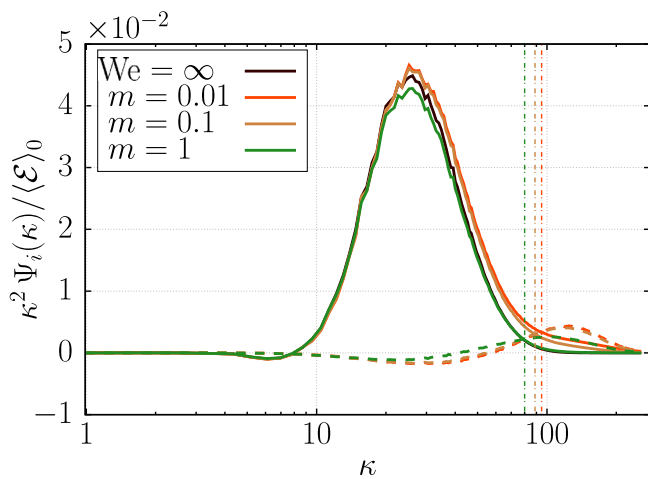
This correlation is similar to one of those presented in McCaslin and Desjardins (2014), and the only difference is that we adopt the Taylor microscale into the energy balance. We evaluate this correlation for all the investigated cases, and compared it with the original correlation



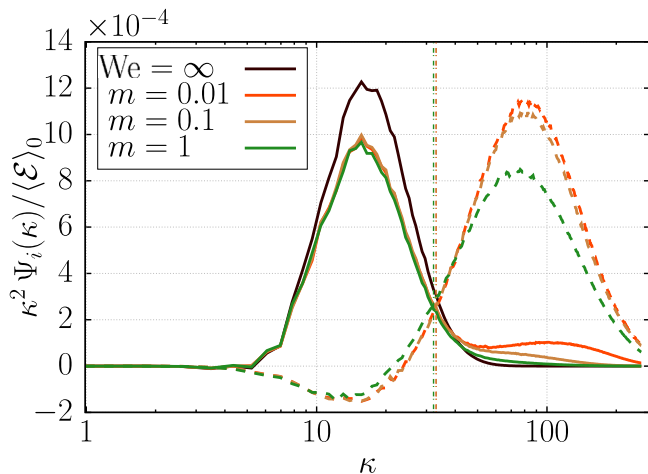
(a)  $m = 0.01, t/\tau_e = 3.7$

(b)  $m = 0.01, t/\tau_e = 22$

Fig. 18. Instantaneous snapshots of interfacial structures for C-7 (with the minimum sheet viscosity) at different times visualized by iso-surfaces of  $\alpha = 0.5$ .



(a)  $t/\tau_e = 3.7$



(b)  $t/\tau_e = 11$

Fig. 19. The spectral rate of entrophy transport by the vortex stretching term  $\Psi_{v,s}$  (solid curves) and surface tension term  $\Psi_\sigma$  (dashed curves) for cases C-6 and C-7 together with C-1 at two instants of time. The values are normalized by the initial domain-averaged entrophy and multiplied by  $\kappa^2$  for better visibility. The vertical dashed-dotted lines indicate  $\kappa_c$  for the case with the same color. The black solid curves show the single-phase results for better comparison. (For interpretation of the references to color in this figure legend, the reader is referred to the web version of this article.)

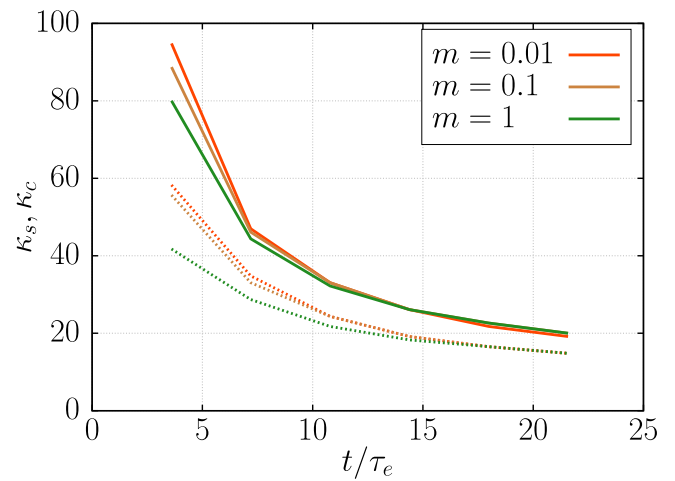
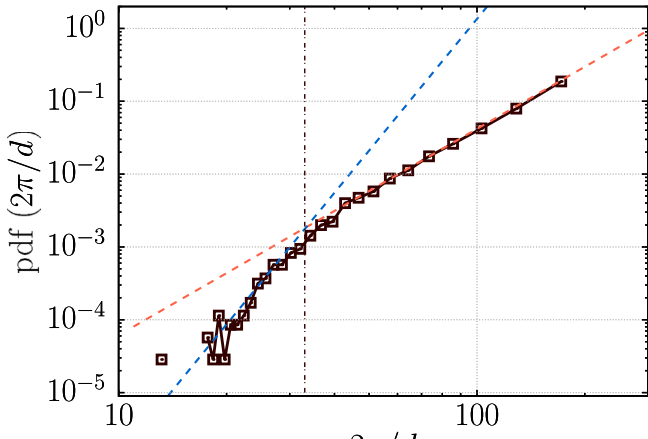


Fig. 20. Temporal variation of the characteristic wavenumbers  $\kappa_c$  (solid lines), and  $\kappa_s$  (dotted lines) for cases C-6 and C-7 together with the reference case of C-1.

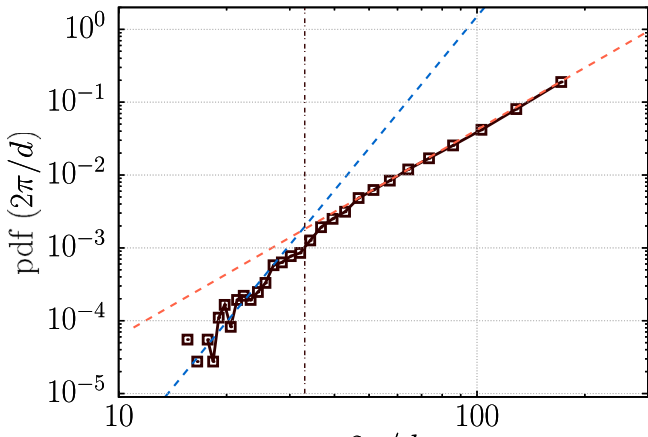
for the Hinze scale (Eq. (8) with  $We_{cr} = 1.17$ ) as well as the length scales associated with the two characteristic wavenumbers presented this work i.e.  $2\pi/\kappa_c$  and  $2\pi/\kappa_s$ .

Figs. 22 to 24 compare these values for the cases C-1 to C-7 separately. It is evident that the proposed correlation based on the Taylor micro-scale perfectly matches the length scale associated with  $\kappa_c$  for most of the cases in the present setup. This, in turn, confirms that  $2\pi/\kappa_c$  is a correct estimation of the maximum size of stable droplets which is associated with the eddies of the size of the Taylor micro-scale, whereas  $2\pi/\kappa_s$  is larger and could act the upper limit for this range. In addition, the original correlation for the Hinze scale results in much smaller values which could be attributed to the different exponent of the dissipation rate in Eq. (8) compared to the proposed correlation.

Nevertheless, for the case C-5 with the higher density ratio presented in Fig. 23(b), the proposed correlation, despite predicting the correct range and trend, overestimates the characteristic length scale associated with  $\kappa_c$ , and is closer to  $2\pi/\kappa_s$ . Given the fact that it also slightly underestimates  $2\pi/\kappa_c$  for the C-4, such a discrepancy might originate in the altered homogeneity of the flow due to the density contrast. This lack of homogeneity could affect the parameters involved in the simple energy balance presented in Eq. (12) i.e.  $\rho$  is not a uniform field and the selected  $u_L$  may also be affected. It has to be further noted that while the approach toward proposing this correlation



(a) C-6



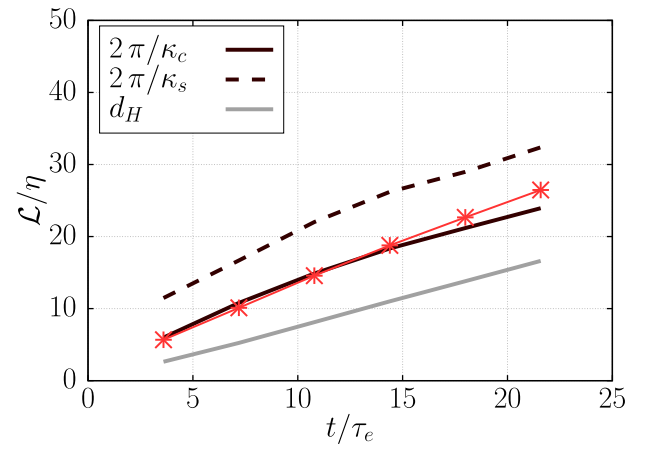
(b) C-7

Fig. 21. Size distribution of droplets at  $t/\tau_e = 11$  for different cases: (a) C-6 and (b) C-7. The vertical dash-dotted lines show the computed  $\kappa_c$  for each case. The blue and red dashed lines are fitted to track the change in the PDF slope. (For interpretation of the references to color in this figure legend, the reader is referred to the web version of this article.)

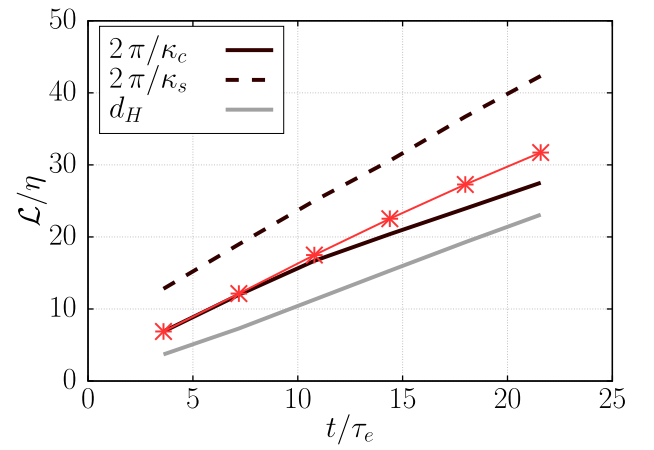
seems general, the choice of characteristic velocity scale remains case-dependent. For the present decaying HIT configuration, the choice of Taylor microscale close to the dissipation range proves to be a valid assumption. Nevertheless, extending this assumption to non-decaying HITs at higher Reynolds numbers may be questionable, and requires further investigation. Therefore, future work will focus on improvement of this correlation concerning other HIT configurations similar to, for instance, the non-decaying HIT presented in [Begemann et al. \(2022\)](#).

### 5. Conclusions

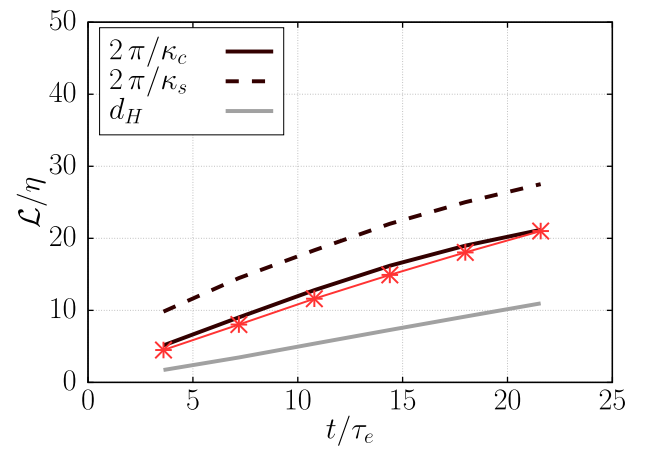
In this study, the turbulence–interface interactions during the fragmentation of a sheet in a freely decaying interfacial HIT are analyzed and interpreted based on the concept of enstrophy transport. Using the fully-resolved volume of fluid simulation of two-phase isotropic turbulence, this approach reveals a clear picture of the scale-dependent role of the surface tension mechanism in energy/enstrophy transport and characterizes the evolution of interfacial turbulence based on its interaction with the vortex stretching mechanism. As an extension to the previous works, we also account for the density and viscosity



(a) C-1



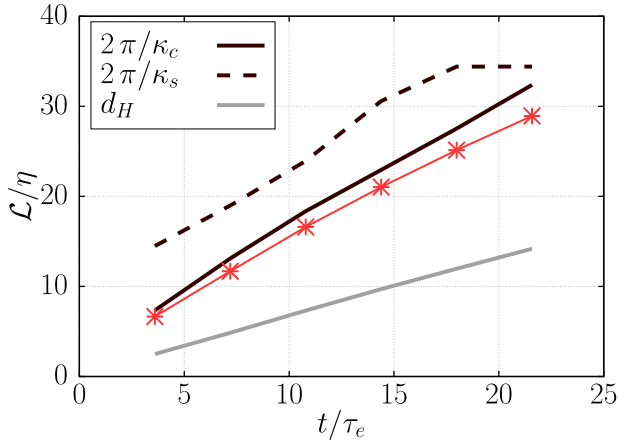
(b) C-2



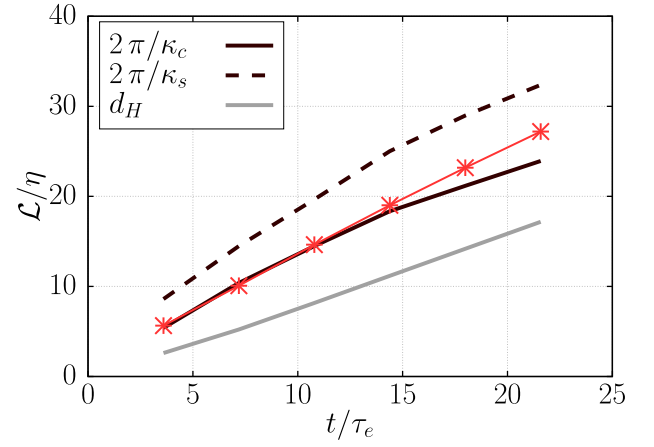
(c) C-3

Fig. 22. The characteristic length scale of the largest stable droplets for C-1 to C-3 over time normalized by the Kolmogorov length scale. The red markers denote the proposed correlation. The solid and dashed black curves indicate length scale associated with  $\kappa_c$  and  $\kappa_s$ , respectively. The gray curve is the original Hinze correlation. (For interpretation of the references to color in this figure legend, the reader is referred to the web version of this article.)

contrasts between the phases as well as the variation of surface tension coefficient. This allows to figure out how they influence the spectral



(a) C-4



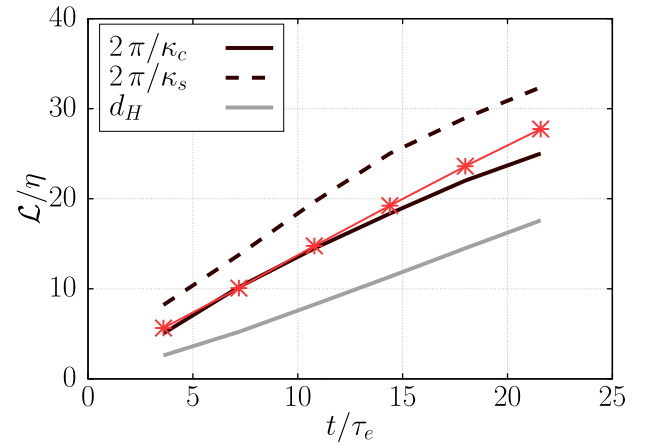
(b) C-5

**Fig. 23.** The characteristic length scale of the largest stable droplets for C-4 and C-5 over time normalized by the Kolmogorov length scale. The red markers denote the proposed correlation. The solid and dashed black curves indicate length scale associated with  $\kappa_c$  and  $\kappa_s$ , respectively. The gray curve is the original Hinze correlation. (For interpretation of the references to color in this figure legend, the reader is referred to the web version of this article.)

and integral trends of individual mechanisms, and eventually shape the dispersed multiphase system.

First, it is demonstrated that the spectral rate of surface tension term has dual contributions to enstrophy transport across the scales. It is negative for larger scales in the wavenumber spectrum and becomes positive for the small scales. Then, two characteristic wavenumbers are identified: (i) a transition wavenumber ( $\kappa_s$ ) at which the surface tension contribution changes the sign from negative to positive, and (ii) a wavenumber ( $\kappa_c$ ) at which the already-positive surface tension rate balances the spectral rate of vortex stretching mechanism. While the former, from a physical point of view, serves at the border between enstrophy-reducing interfacial events (breakup) and enstrophy-generating ones (surface minimization/coalescence), the latter scale corresponds to a similar length scale that the energy cascade of two-phase turbulence deviates from its single-phase similitude. We further connect this characteristic length scale to the statistics of the interfacial structures and observe that the size distribution of droplets changes slope at a similar scale.

The simulation cases are categorized into three groups to investigate the effect of Weber number, density ratio, and viscosity ratio separately. For each group, we analyzed the temporal variation of integral quantities such as domain-averaged enstrophy and total interfacial area.



(a) C-6

**Fig. 24.** The characteristic length scale of the largest stable droplets for C-6 and C-7 over time normalized by the Kolmogorov length scale. The red markers denote the proposed correlation. The solid and dashed black curves indicate length scale associated with  $\kappa_c$  and  $\kappa_s$ , respectively. The gray curve is the original Hinze correlation. (For interpretation of the references to color in this figure legend, the reader is referred to the web version of this article.)

Then, we explore the trends in spectral space. The analysis discloses that increasing sheet Weber number by lowering the surface tension coefficient, increasing density, and decreasing the viscosity of the sheet all enhance the vortex stretching effect across the scales and dilate the spectral range at which the surface tension contribution is negative toward the smaller scales, and thus facilitate the fragmentation. Whereas the higher surface tension coefficient, higher viscosity, and lower density ratio expand the spectral range associated with the positive contribution of surface tension toward the larger scales, and suppress fragmentation events. These trends are also consistent with different works in the existing literature. We also examined the temporal variation of the aforementioned characteristic length scales for each group, and show that for the present decaying HIT they eventually converge. Nevertheless, at the early stages of the flow, they yield a large difference, indicating the probability of generating semi-stable droplets. Then, we argue that for this decaying HIT problem the Hinze scale should correspond to a range between  $2\pi/\kappa_c$  and  $2\pi/\kappa_s$ , as the turbulent breakup is stopped for droplets smaller than this range. Based on this new interpretation, and using the concept of Taylor micro-scale and energy balance for small-scale motions, a correlation is derived for the largest stable droplets needless to any tuning parameter. The

results match the  $2\pi/\kappa_c$  for most of the cases confirming its relevance to representing the Hinze scale in numerical simulations.

As another essential conclusion, we should emphasize the choice of proper interfacial HIT configuration for future research. The present study has employed a HIT configuration consisting of a thin sheet placed in the middle of the box that is chosen to be consistent with the previous works in the literature (Trontin et al., 2010; Saeedipour and Schneiderbauer, 2021). But it brings advantages and disadvantages. For instance, the sheet is initially at rest and the fragmentation starts from a realistic condition with no initial influence of the surface tension compared to a setup with dispersed spherical droplets. Nevertheless, as a disadvantage, such an initial condition poses questions about the homogeneity assumption. In fact, as the interface propagates in perpendicular direction to the sheet, the energy spectra vary depending on the distance to the center of the box. We have analyzed the 2D energy spectra as well as spectral enstrophy rates on different planes in the  $y$ -direction (not presented here), and have observed a similar trend for  $\kappa_c$  at each 2D plane. It could be observed that the interface propagation in the  $y$ -direction still follows the general physics that is disclosed about the turbulence–interface interactions; however, the slight variation in characteristic wavenumbers in each 2D plane in the  $y$ -direction compared to the other two homogeneous directions could pose uncertainty on the exact values that contribute to the calculation of  $\kappa_c$  by 3D shell-averaged spectral analysis. The uncertainty quantification of such effect, however, requires a more thorough analysis which was not in the scope of the present study and remains for future works. Besides, a more homogeneous initial condition for the interface similar to recent works of Crialesi-Esposito et al. (2022) and Begemann et al. (2022) i.e. comprising a distribution of multiple large drops at the beginning could prevent such uncertainty when performing 3D shell-averaged spectral analysis, and enables computation of unambiguous characteristic wavenumbers.

The findings of the present study stimulate future research in two possible directions of physics and modeling: (i) further evaluation of this enstrophy-based approach and the connection to the size distribution of droplets in a more statistically-steady setup such as non-decaying HIT with an initial condition that preserves the homogeneity of interface propagation. Here, focusing on the interfacial events within the range of  $\kappa_s$  to  $\kappa_c$ , and the stability of droplets could be a valid direction for the future research. Also, the role of other terms in the enstrophy equation e.g. the baroclinic torque during the evolution of interfacial turbulence with density contrast may be more investigated. (ii) Improving the proposed correlation for the Hinze scale, and developing new functional SGS models for surface tension force in the context of two-phase LES based on the enstrophy transport equation. For the former, a non-decaying HIT configuration could be more pertinent, while for the latter, the present fully-resolved simulations could serve as the basis for a-priori tests of the new models.

#### CRediT authorship contribution statement

**Mahdi Saeedipour:** Conceptualization, Methodology, Investigation, Data curation, Formal analysis, Software, Writing – original draft.

#### Declaration of competing interest

The authors declare that they have no known competing financial interests or personal relationships that could have appeared to influence the work reported in this paper.

#### Data availability

Data will be made available on request

#### Acknowledgments

The author acknowledges the funding support from K1-MET GmbH, the metallurgical competence center in Austria which is supported by the COMET program (Competence Center for Excellent Technologies) with the grant number 869295. The author also thanks Dr. Simon Scheniderbauer (Johannes Kepler University) for the fruitful scientific discussions.

#### References

- Begemann, A., Trummer, T., Trautner, E., Hasslberger, J., Klein, M., 2022. Effect of turbulence intensity and surface tension on the emulsification process and its stationary state – A numerical study. *Can. J. Chem. Eng.* 100, 3548–3561.
- Brackbill, J.U., Kothe, D.B., Zemach, C., 1992. A continuum method for modeling surface tension. *J. Comput. Phys.* 100 (2), 335–354.
- Crialesi-Esposito, M., Chibbaro, S., Brandt, L., 2023. The interaction of droplet dynamics and turbulence cascade. *Commun. Phys.* 6, 1–8.
- Crialesi-Esposito, M., Rosti, M.E., Chibbaro, S., Brandt, L., 2022. Modulation of homogeneous and isotropic turbulence in emulsions. *J. Fluid Mech.* 940, 1–37.
- Deane, G.B., Stokes, M.D., 2002. Scale dependence of bubble creation mechanisms in breaking waves. *Nature* 418, 839–844.
- Denaro, F.M., 2018. What is the basic physical meaning of enstrophy? URL [https://www.researchgate.net/post/What\\_is\\_the\\_basic\\_physical\\_meaning\\_of\\_enstrophy](https://www.researchgate.net/post/What_is_the_basic_physical_meaning_of_enstrophy).
- Dodd, M.S., Ferrante, A., 2016. On the interaction of Taylor length scale size droplets and isotropic turbulence. *J. Fluid Mech.* 806, 356–412.
- Estivaleres, J.-L., Aniszewski, W., Auguste, F., Ling, Y., Osmar, L., Caltagirone, J.-P., Chirco, L., Pedrono, A., Popinet, S., Berlemont, A., Magnaudet, J., Ménard, T., Vincent, S., Zaleski, S., 2022. A phase inversion benchmark for multiscale multiphase flows. *J. Comput. Phys.* 450, 110810.
- Gamet, L., Scala, M., Roenby, J., Scheuffer, H., Pierson, J.-L., 2020. Validation of volume-of-fluid openFOAM isoAdvector solvers using single bubble benchmarks. *Comput. & Fluids* 213, 104722.
- Garrett, C., Li, M., Farmer, D., 2000. The connection between bubble size spectra and energy dissipation rates in the upper ocean. *J. Phys. Oceanogr.* 30, 2163–2171.
- Hasslberger, J., Ketterl, S., Klein, M., 2020. A-priori assessment of interfacial sub-grid scale closures in the two-phase flow LES context. *Flow Turbul. Combust.* 105, 359–375.
- Hasslberger, J., Klein, M., Chakraborty, N., 2018. Flow topologies in bubble-induced turbulence: a direct numerical simulation analysis. *J. Fluid Mech.* 857, 270–290.
- Hinze, J.O., 1955. Fundamentals of the hydrodynamic mechanism of splitting in dispersion processes. *AIChE J.* 1, 289–295.
- Jofre, L., Dodd, M.S., Grau, J., Torres, R., 2020. Near-interface flow modeling in large-eddy simulation of two-phase turbulence. *Int. J. Multiph. Flow.* 132, 103406.
- Klein, M., Ketterl, S., Hasslberger, J., 2019. Large eddy simulation of multiphase flows using the volume of fluid method: Part 1—Governing equations and a priori analysis. *Exp. Comput. Multiph. Flow* 1, 130–144.
- Li, Z., Jaber, F.A., 2009. Turbulence-interface interactions in a two-fluid homogeneous flow. *Phys. Fluids* 21, 095102.
- Ling, Y., Zaleski, S., Scardovelli, R., 2015. Multiscale simulation of atomization with small droplets represented by a Lagrangian point-particle model. *Int. J. Multiph. Flow.* 76, 122–143.
- Mangani, F., Soligo, G., Roccon, A., Soldati, A., 2022. Influence of density and viscosity on deformation, breakage, and coalescence of bubbles in turbulence. *Phys. Rev. Fluids* 7.
- McCaslin, J.O., Desjardins, O., 2014. Theoretical and Computational Modeling of Turbulence/Interface Interactions. Tech. rep., Center for Turbulence Research.
- McComb, W.D., 1992. *The Physics of Fluid Turbulence*. Oxford University Press.
- Pope, S.B., 2000. *Turbulent Flows*. Cambridge University Press, Cambridge, UK.
- Roenby, J., Bredmose, H., Jasak, H., 2016. A computational method for sharp interface advection. *R. Soc. Open Sci.* 3, 160405.
- Saeedipour, M., Pirker, S., Bozorgi, S., Schneiderbauer, S., 2016. An Eulerian-Lagrangian hybrid model for the coarse-grid simulation of turbulent liquid jet breakup. *Int. J. Multiph. Flow.* 82, 17–26.
- Saeedipour, M., Schneiderbauer, S., 2019. A new approach to include surface tension in the subgrid eddy viscosity for the two-phase LES. *Int. J. Multiph. Flow.* 121, 103128.
- Saeedipour, M., Schneiderbauer, S., 2021. Favre-filtered LES-VOF of two-phase flows with eddy viscosity-based subgrid closure models: An a-posteriori analysis. *Int. J. Multiph. Flow.* 144, 103780.
- Saeedipour, M., Schneiderbauer, S., 2022. Toward a universal description of multiphase turbulence phenomena based on the vorticity transport equation. *Phys. Fluids* 34, 073317.
- Saeedipour, M., Schneiderbauer, S., Ploh, G., Brenn, G., Pirker, S., 2017. Multiscale simulations and experiments on water jet atomization. *Int. J. Multiph. Flow.* 95, 71–83.
- Saeedipour, M., Vincent, S., Estivaleres, J.L., 2021. Toward a fully resolved volume of fluid simulation of the phase inversion problem. *Acta Mech.* 232, 2695–2714.

- Saeedipour, M., Vincent, S., Pirker, S., 2019. Large eddy simulation of turbulent interfacial flows using approximate deconvolution model. *Int. J. Multiph. Flow.* 112, 286–299.
- Scheufler, H., Roenby, J., 2019. Accurate and efficient surface reconstruction from volume fraction data on general meshes. *J. Comput. Phys.* 383, 1–23.
- Schneiderbauer, S., Saeedipour, M., 2022. The impact of interphase forces on the modulation of turbulence in multiphase flows. *Acta Mech. Sinica* 38, 721446.
- Skartlien, R., Sollum, E., Schumann, H., 2013. Droplet size distributions in turbulent emulsions: Breakup criteria and surfactant effects from direct numerical simulations. *J. Chem. Phys.* 139, 174901.
- Tennekes, H., Lumley, J.L., 1972. *A First Course in Turbulence*. The MIT Press.
- Trontin, P., Vincent, S., Estivalezes, J.L., Caltagirone, J.P., 2010. Direct numerical simulation of a freely decaying turbulent interfacial flow. *Int. J. Multiph. Flow.* 36, 891–907.
- Villermaux, E., 2007. Fragmentation. *Annu. Rev. Fluid Mech.* 39, 419–446.
- Vincent, S., Tavares, M., Fleau, S., Mimouni, S., Ould-Rouiss, M., Estivalezes, J.L., 2018. A priori filtering and LES modeling of turbulent two-phase flows application to phase separation. *Comput. & Fluids* 176, 245–259.
- Weller, H., Tabor, G., Jasak, H., Fureby, C., 1998. A tensorial approach to computational continuum mechanics using object-oriented techniques. *Comput. Phys.* 12, 620–631.
- Yu, H., Girimaji, S.S., Luo, L.-S., 2005. Lattice Boltzmann simulations of decaying homogeneous isotropic turbulence. *Phys. Rev. E* 71, 016708.
- Zhang, G., Chanson, H., 2019. On void fraction and flow fragmentation in two-phase gas-liquid free-surface flows. *Mech. Res. Commun.* 96, 24–28.